

Porosity and Permeability Prediction through Forward Stratigraphic Simulations Using GPMTM and PetrelTM: Application in Shallow Marine Depositional Settings.

Daniel Otoo and David Hodgetts

Department of Earth and Environmental Sciences, University of Manchester, Manchester, M13 9PL, United Kingdom.

Correspondence to: Daniel Otoo (daniel.otoo@manchester.ac.uk)

Abstract

The forward stratigraphic simulation approach is applied to forecast porosity and permeability trends in the Volve field subsurface model. Variograms and synthetic well logs from the forward stratigraphic model were combined with known data to guide porosity and permeability distribution. Building a reservoir model that fits data at different locations comes with high levels of uncertainty. Therefore, it is critical to generate an appropriate stratigraphic framework to guide lithofacies and associated petrophysical distribution in a subsurface model. The workflow adopted is in three parts; first, simulation of twenty scenarios of sediment transportation and deposition using the geological process modeling (GPMTM) software developed by Schlumberger. Secondly, an estimation of the extent and proportion of lithofacies proportions in the stratigraphic model using the property calculator tool in PetrelTM. Finally, porosity and permeability values were assigned to corresponding lithofacies-associations in the forward stratigraphic model to produce a forward stratigraphic-based porosity and permeability model. Results show a lithofacies distribution model, which depends on sediment diffusion rate, sea level variation, flow rate, wave processes, and tectonic events. This observation is consistent with the natural occurrence, where variation in sea level, sediment supply, and accommodation control stratigraphic sequences. Validation wells, VP1 and VP2 located in the original Volve field model and the forward stratigraphic-based models show a significant similarity, especially in the porosity models. These results suggest that forward stratigraphic simulation outputs can be used together with geostatistical modeling workflows to improve subsurface property representation in reservoir models.

1 **Introduction**

2 The distribution of reservoir properties such as porosity and permeability is a direct function of a complex
3 combination of sedimentary, geochemical, and mechanical processes (Skalinski & Kenter, 2014). The
4 impact of reservoir petrophysics on well planning and production strategies makes it imperative to use
5 reservoir modeling techniques that present realistic property variations via 3-D models (Deutsch and
6 Journel, 1999; Caers and Zhang, 2004; Hu & Chugunova, 2008). Typically, reservoir modeling requires
7 continued property modification until an appropriate match to subsurface data. Meanwhile, subsurface
8 data acquisition is expensive, thus restricts data collection and accurate subsurface property modeling.
9 Several studies, Hodgetts et al. (2004) and Orellana et al. (2014) have demonstrated how stratigraphic
10 patterns, and therefore petrophysical attributes in seismic data, outcrops, and well logs are applicable in
11 subsurface modeling. However, the absence of detailed 3-dimensional depositional frameworks to guide
12 property modeling inhibits this strategy (Burgess et al. 2008). Reservoir modeling techniques with the
13 capacity to integrate forward stratigraphic simulation outputs with stochastic modeling techniques for
14 subsurface property modeling will improve reservoir heterogeneity characterization, because they more
15 accurately produce geological realism than the other modeling methods (Singh et al. 2013). The use of
16 geostatistical-based methods to represent spatial variability of reservoir properties has been in many
17 exploration and production projects (Kelkar and Godofredo, 2002). In the geostatistical modeling method,
18 an alternate numerical 3-D model (realizations) shows different property distribution scenarios that are
19 most likely to match well data (Ringrose & Bentley, 2015). However, due to cost reservoir modeling
20 practitioners continue to encounter the challenge of obtaining adequate subsurface data to deduce reliable
21 variograms for subsurface modeling, therefore introducing a significant level of uncertainty in reservoir
22 models (Orellana et al. 2014). The advantages of applying geostatistical modeling approaches to represent
23 reservoir properties in models are discussed in studies by Deutsch and Journel (1999), Dubrule, (1998).
24 A notable disadvantage is that the geostatistical modeling method tends to confine reservoir property
25 distribution to subsurface data and rarely produces geological realism to capture sedimentary events that
26 led to reservoir formation (Hassanpour et al. 2013). In effect, the geostatistical modeling technique does

not reproduce long-range continuous reservoir properties, which are essential for generating realistic reservoir connectivity models (Strebelle & Levy, 2008). The forward stratigraphic simulation approach was applied in this contribution to forecast lithofacies, porosity, and permeability in a reservoir model, based on lessons from Otoo and Hodgetts (2019). A significant aspect of this work is using variogram parameters from forward stratigraphic-based synthetic wells to simulate porosity and permeability trends in the reservoir model. Forward stratigraphic modeling involves morphodynamic rules to replicate 3-dimensional stratigraphic depositional trends observed in data (e.g. seismic). Forward stratigraphic modeling operates on the guiding principle that multiple sedimentary process-based simulations in a 3-D framework will improve facies, and therefore petrophysical property distribution in a geological model. The geological process modeling GPMTM software (Schlumberger, 2017), which operates on forward stratigraphic simulation principles, replicates a depositional sequence to provide a 3-dimensional framework to predict porosity, permeability in the study area. The reservoir interval under study is within the Hugin formation. Studies by Varadi et al. (1998); Kieft et al. (2011) indicate that the Hugin formation consists of a complex depositional architecture of waves, tidal, and fluvial processes. This knowledge suggests that a single depositional model will not be adequate to produce a realistic lithofacies or petrophysical distributions model of the area. Furthermore, the complicated Syn-depositional rift-related faulting system, significantly influences the stratigraphic architecture (Milner and Olsen, 1998). Therefore, the focus here is to produce a depositional sequence, which captures subsurface attributes observed in seismic and well data to guide property modeling.

Study Area

The Volve field (Figure 1), located in Block 15/9 south of the Norwegian North Sea, has the Hugin Formation as the reservoir interval from which hydrocarbons are produced (Vollset and Dore, 1984). The Hugin formation, which is Jurassic in age (late Bajocian to Oxfordian), is made up of shallow marine to marginal marine sandstone deposits, coals, and a significant influence of wave events that tend to control lithofacies distribution in the formation (Varadi et al. 1998; and Kieft et al. 2011). Studies by Sneider et al. (1995) and Husmo et al. (2003) associate sediment deposition into the study area to rift-related

53 subsidence and successive flooding during a large transgression of the Viking Graben within the Middle
54 to Late Jurassic period. Also, Cockings et al. (1992), Milner and Olsen (1998) indicate that the Hugin
55 formation comprises of marine shoreface, lagoonal and associated coastal plain, back-stepping delta-
56 plain, and delta front. However, recent studies by Folkestad and Satur (2006) also provide evidence of a
57 high tidal event, which introduces another dimension that requires attention in any subsurface modeling
58 task in the study area. The thickness of the Hugin formation is estimated between 5 m and 200 m, but can
59 be thicker off-structure and non-existent on structurally high segments due to post-depositional erosion
60 (Folkestad and Satur, 2006).

61 A summarised sedimentological delineation within the Hugin formation is derived based on studies by
62 Kieft et al. (2011). In **Table 1**, lithofacies-association codes A, B, C, D, and E represent bay fill units,
63 shoreface sandstone facies, mouth bar units, fluvio-tidal channel fill sediments, and coastal plain facies
64 units, respectively. Additionally, a lithofacies association prefixed code F, which consists of open marine
65 shale units, mudstone. Within it are occasional siltstone beds, parallel laminated soft sediment
66 deformation that locally develop at bed tops. The lateral extent of the code F lithofacies package in the
67 Hugin formation is estimated to be 1.7 km to 37.6 km, but the total thickness of code F lithofacies is not
68 known (Folkestad & Satur, 2006).

69 **Data and Software**

70 This work is based on the description and interpretation of petrophysical datasets in the Volve field by
71 Equinor. Datasets include 3-D seismic and a suite of 24 wells that consist of formation pressure data, core
72 data, petrophysical and sedimentological logs. Previous studies by Folkestad & Satur (2006) and Kieft et
73 al., (2011) in this reservoir interval show varying grain size, sorting, sedimentary structures, bounding
74 contacts of sediment matrix. Grain size, sediment matrix, and the degree of sorting will typically drive
75 the volume of the void created, and therefore the porosity and permeability attributes. Wireline-log
76 attributes such as gamma-ray (GR), sonic (DT), density (RHOB), and neutron-porosity (NPHI)
77 distinguish lithofacies units, stratigraphic horizons, and zones that are essential for building the 3-D
78 property model in Schlumberger's PetrelTM software. Besides, this study also seeks to produce a realistic

79 depositional model like the natural stratigraphic framework in a shallow marine depositional setting.
80 Therefore, obtaining a 3-dimensional stratigraphic model that shows a similar stratigraphic sequence
81 observed in the seismic data allows us to deduce variogram parameters to serve as input in actual
82 subsurface property modeling.

83 Twenty forward stratigraphic simulations were produced in the geological process modeling (GPM™)
84 software to illustrate depositional processes that resulted in the build-up of the reservoir interval under
85 study. By the fourth simulation, there was a development of stratigraphic patterns that shows similar
86 sequences as those observed in seismic, hence the decision to constrain the simulation to twenty scenarios.
87 Delft3D-Flow™; Rijin & Walstra, (2003); DIONISOS™; Burges et al. (2008) are examples of subsurface
88 process modeling software used in similar studies. The availability of the GPM™ software license and
89 the capacity to integrate stratigraphic simulation outputs in the property modeling workflow in Petrel™
90 is the reason for using the geological process modeling software in this study.

91 **Methodology**

92 The workflow (Figure 2a) combines the stratigraphic simulation capacity of GPM™ in different
93 sedimentary processes and the property modeling tools in Petrel™ to predict the distribution of porosity
94 and permeability properties away from known data. This involves three broad steps: (i) forward
95 stratigraphic simulation in GPM™ (2019.1 version), (ii) lithofacies classification using the calculator tool
96 in Petrel™, and (iii) porosity and permeability modeling in Petrel™ (2019.1 version).

97 **Forward Stratigraphic Simulation in GPM™**

98 GPM™ is commercial software developed by Schlumberger to simulate clastic and carbonate
99 sedimentation in a deep or shallow marine environment. GPM™ consists of geological processes such as
100 steady flow, sediment diffusion, tectonics, and sediment accumulation that rely on physical equations and
101 assumptions to replicate the process of sedimentation in a geological basin. A realistic realization of a
102 stratigraphic pattern as observed in seismic or well data provides a 3-dimensional framework to constrain
103 subsurface property representation that conforms with the real-world property distribution trends. In

104 clastic sedimentation, the movement of sediments relies on equations from the original SEDSIM
105 developed in Stanford University (Harbaugh, 1993). Sediment movement, erosion, and deposition is
106 governed by a simplified Navier Stokes equation. “Simplified” because the Navier-Stokes equation in its
107 original form define sediment movement in a 3-dimensions differential form, while the flow equation in
108 GPMTM is 2-dimensional with an arbitrary input of flow depth. Kieft et al. (2011) describe the influence
109 of a combination of fluvial and wave processes in the genetic structure of sediments in the Hugin
110 formation. These geological processes are rapid, depending on accommodation generated by sea-level
111 variation and or sediment composition and flow intensity. The deposition of sediments into a geological
112 basin and its response to post-depositional sedimentary or tectonic processes are significant in the ultimate
113 distribution of subsurface lithofacies and petrophysics. Therefore, several input parameters for the
114 forward simulation to attain a stratigraphic output that fits existing knowledge of paleo-sediment
115 transportation and deposition into the study area (see Table 2). The forward simulation at all stages
116 portrayed geological realism concerning stratigraphic sequence, but it also revealed some limitations,
117 such as instability in the simulator when more than three geological processes run concurrently. Given
118 this, the diffusion and tectonic processes remained constant whiles varying the steady flow, unsteady
119 flow, and sediment accumulation processes in each simulation run.

120 **Steady & Unsteady Flow Process**

121 The steady flow process in GPM simulates flows that change slowly over a period, or sediment transport
122 scenarios where flow velocity and channel depth do not vary abruptly e.g. rivers at a normal stage, deltas,
123 and sea currents. Considering the influence of fluvial activities during sedimentation in the Hugin
124 formation, it is significant to capture its impact on the resultant simulated output.

125 The unsteady flow process can simulate periodic flows such as turbidites where the occurrence is not
126 regular, and the velocity of flow changes abruptly over time. The unsteady flow process applies several
127 fluid elements driven by gravity and friction against the hypothetical topographic surface. Otoo and
128 Hodgetts (2019) illustrate how the unsteady process in GPMTM attains realistic distribution of lithofacies
129 units in a turbidite fan system. Although the steady and unsteady flow governing equations distantly rely

on the Navier-Stokes equations, the steady flow is quite distinct, as it uses a finite difference numerical method for faster computation and to also illustrate the frequency of flow that is characteristic in channel flow such as rivers. The finite difference method applies an assumption that flow velocity is constant from channel bottom to surface. In contrast, the unsteady flow uses the particle method from SEDSIM3 to solve the sediment concentration in flow and sediment transport capacity (Tetzlaff & Harbaugh 1989). The simplified equation in GPMTM attempts to solve the problem of “shallow-water free-surface flow” over an arbitrary topography surface (Tetzlaff, D. personal communication, February 2021). “Shallow water” indicates the instance where only the vertically-averaged flow velocity and flow depth are applied and kept track of as a function of two horizontal coordinates.

The equation that control steady and unsteady flow is expressed through:

$$\frac{\partial h}{\partial t} + \nabla \cdot hQ = 0 \quad (1)$$

Where: h is flow depth, t is time, and Q the horizontal flow velocity vector.

$$\left(\frac{\partial Q}{\partial t}\right) = -(g\nabla)H + \frac{c_2}{\rho} \nabla^2 Q - \frac{c_2 Q/Q/h}{h} \quad (2)$$

Where: $\frac{\partial Q}{\partial t}$ is the Lagrangian derivative of flow relative to time, g is gravity, H is the water surface elevation, c_2 is the fluid friction coefficient, ρ is the water density, c_1 is the water friction coefficient and h is the flow depth.

The Manning’s equation is applied to relate flow, slope, flow depth and hydraulic radius channels with a constant cross-section for the steady flow process. Manning’s formula states:

$$V = \frac{k}{n} R_h^{2/3} S^{1/2} \quad (3)$$

Where: V is the flow velocity, k is the unit conversion factor, n is the Manning’s coefficient which depends on channel rugosity, R_h is the hydraulic radius and S is the slope.

As mentioned earlier, the unsteady flow process uses the particle method equation, which relies on the assumption that erosion and deposition depend on the balance between the flow’s transport capacity and

153 the “effective sediment concentration”. The equation for multiple-sediment transport in flow is given as
 154 follows:

$$155 \quad A_{em} = \sum_{k_s} \frac{l_{Ks}}{f_{1k_s}} \quad (4)$$

156 Where: A_{em} is the effective sediment concentration of mixture, l_{ks} is the sediment concentration of each
 157 type, and f_{1,k_s} is the transportability of each sediment type.

158 The transport capacity of a sediment type is expressed by equations (5) and (6). Let consider

$$159 \quad R = (A - A_{em})f_{2,k_s} \quad (5)$$

160 Where f_{2,k_s} is the erosion-deposition rate coefficient for sediment type k_s . For every sediment type k_s ,
 161 the formula for transporting sediment of different grain sizes is given as:

$$162 \quad (H - Z) \frac{Dl_{Ks}}{Dt} = \begin{cases} R & \text{if } R > 0 \text{ and } \tau_0 \geq f_{3,k_s} \text{ and } k(x, y, z) = K_s \\ & \text{or } R < 0 \text{ and } K_s = 1 \text{ or } l_{k_s-1} = 0 \\ 0 & \text{otherwise} \end{cases} \quad (6)$$

163 Where;

164 H is the free surface elevation to sea level, Z is the topographic elevation for sea level, K_s is the sediment
 165 type, l_{ks} is the volumetric sediment concentration of a specific type (k).

166 **Sediment Diffusion Process**

167 The diffusion process replicates sediment movement from a higher slope (source location) and deposition
 168 into a lower elevation of the model area. Sediment diffusion runs on the assumption that sediments are
 169 transported downslope at a proportional rate to the topographic gradient, making fine-grained sediments
 170 easily transportable than coarse-grained sediments. Sediment diffusion depends on three parameters: (i)
 171 sediment grain size and turbulence in the flow, (ii) diffusion curve that serves as a unitless multiplier in
 172 the algorithm and, (iii) diffusion coefficient. The diffusion coefficient depends, among other variables on
 173 the type of sediment and “energy” of the depositional environment. In this contribution, the highest depth-

174 dependent diffusion coefficient occurs near sea level, where the “energy” is highest over a geological
175 time (Dashtgard et al. 2007).

176 In GPMTM, sediment diffusion is calculated using a simplified expression:

$$177 \quad \frac{\partial z}{\partial t} = D_i \nabla^2 z + S_n \quad (7)$$

178 where z is topographic elevation, D_i is the diffusion coefficient, t for time, and $\nabla^2 z$ is the laplacian of z ,
179 and S_n is the sediment source term.

180 Sediment diffusion (D_i) is estimated by assuming that the grain size for each sediment component (coarse
181 sand, fine sand, silt, and clay) are known. Also an assumption that these sediment types have a uniform
182 diameter (D) in the flow mix (Dade & Friend 1998; and Zhong 2011). In that case, external fore (F_e),
183 which consist of drag, lift, virtual mass, and Basset history force is given as:

$$184 \quad F_e = \alpha_e M_e + \alpha_e \Phi_D \cdot \frac{U_{fi} - U_{ei}}{T_p} \quad (8)$$

185 M_e is the resultant force of other forces with the exception of drag force, T_p stokes relation time, expressed
186 as: $T_p = \rho_p D^2 / (18 \rho_f \nu_f)$, with ρ_f and ν_f as density and viscosity of fluid respectively. Φ_D is a coefficient
187 that accounts for the non-linear dependence of drag force on grain slip Reynolds number (R_p).

$$188 \quad \Phi_D = \frac{R_p}{24} C_D \quad (9), \text{ with } C_D \text{ sediment grain coefficient.}$$

189 With the flow component in place, the diffusion coefficient (D_i) is deduced from the Einstein equation.
190 Using an assumption that the diffusion coefficient decreases with increasing grain size and rise in
191 temperature, and that the coefficient f is known, the expression for D_i is:

$$192 \quad D_i = \frac{K_B \cdot T}{f} \quad (10)$$

193 Meanwhile, f is a function of the dimension of the spherical particle involved at a particular time (t). In
194 accounting for f , the equation for D_i changes into:

$$195 \quad D_i = \frac{K_B \cdot T}{6 \cdot \pi \cdot \eta_o \cdot r} \quad (11)$$

196 **Sediment Accumulation**

197 The sediment accumulation process in GPM is designed to generate an arbitrary amount of sediment
198 representing the artificial vertical thickness of a lithology as interpreted in a well or outcrop data (Tetzlaff,
199 D., personal communication, February 2021). The areal input rates for each sediment type (coarse-
200 grained, fine-grained sediments) use the value of the map surface at each cell in the model and multiply
201 it by a value from a unitless curve at each time step in the simulation to estimate the thickness of sediments
202 accumulated or eroded from a cell in the model. Sediment accumulation in the GPM software requires
203 other processes such as steady flow and diffusion to account for sediment transport (sediment entering or
204 leaving a cell) before a deposition/year (mm/yr) function to artificially produce the height of sediment
205 deposited per cell. The accumulation of sediments in GPM is expressed as:

$$206 \quad A_T = \sum_{S=1}^n [(M_{v1} * S_{c1}), \dots, n] \quad (12)$$

207 Where;

208 A_T is the total sediment accumulated in a cell over a period, S is the sediment type, M_v is the map value
209 of sediment in each cell, and S_C is the sediment supply curve as a function of topographic elevation.

210 **Boundary Conditions for Forward Stratigraphic Simulation**

211 Realistic reproduction of stratigraphic patterns in the model area requires input parameters (initial
212 conditions), such as paleo-topography, sea-level curves, sediment source location, and distribution curve,
213 tectonic event maps (subsidence and uplift), and sediment mix velocity. The application of these input
214 parameters in GPMTM and their impact on the resultant stratigraphic framework is below.

215 **Hypothetical Paleo-Surface:** The hypothetical paleo-topographic for the stratigraphic simulation is from the
216 seismic data (Figure 3), using the assumption that the present day stratigraphic surface (paleo shoreline in Figure
217 4a) occurred as a result of basin filling over geological time. Since the surface obtained from the seismic section
218 have undergone various phases of subsidence and uplifts, it is significant to note that the paleo topographic surface
219 used in this work does not represent an accurate description of the basin at the period of sediment deposition; thus
220 presenting another level of uncertainty in the simulation. To derive an appropriate paleo-topographic for this

task, five paleo topographic surfaces (TPr) were generated, by adding or subtracting elevations from the inferred paleo topographic surface (see Figure 4g) using the equation:

$$TPr = Sbs + EM \quad (13)$$

where, Sbs is the base surface scenario (in this instance, scenario 6), and EM an elevation below and above the base surface.

The paleo-topographic surface in scenario 3 (figure 4d) is selected because it produced a stratigraphic sequences that fit the depositional patterns interpreted from the seismic section (Figure 5d).

Sediment Source Location: Based on regional well correlations in Kieft et al. 2011, and seismic interpretation of the basin structure, the sediment entry point is placed in the north-eastern section of the hypothetical paleo-topography surface. The exact sediment entry point into this basin is unknown, so three entry points were placed at a 4 km radius around the primary location (Figure 3c) to capture possible sediment source locations in the model area. The source position is a positive integer (values greater than zero) to enable sediment movement to other parts of the topographic surface.

Sea Level: The sea-level curve is deduced from published studies and facies description in shallow marine depositional environments (e.g. Winterer and Bosellini, 1981). To sea level was constrained 30 m for short simulation runs (5000 to 20000 years), but varied with the increasing duration of the simulation (see Table 2). The peak sea-level in the simulation depicts the maximum flooding surface (Figure 5d), and therefore the inferred sequence boundary in the geological process model.

Diffusion and Tectonic Event Rates: The sediment mix proportion, diffusion rate, and tectonic event functions are from studies such as Walter, (1978), Winterer and Bosellini, (1981), and Burges et al., (2008). The diffusion and tectonic event rates were increased or reduced to produce a stratigraphic model that fit our knowledge of basin evolution in the study area. For example, in scenario 1 (Figure 6a), the early stages of clinoform development show resemblance to interpreted trends in the seismic section (**Figure 3b**). The process commenced with a diffusion coefficient of 8 m²/a, but it varied at each scenario to obtain diffusion coefficients to improve the model. Excluding the initial topography (Figure 4d), input

parameters in geological processes such as wave events, steady/unsteady flow, diffusion, and tectonic events used curve functions to provide variations in the simulation.

The sensitivity of input parameters in the forward stratigraphic simulation is notable when there is a change of value in sediment diffusion, and tectonic rates or dimension of the hypothetical topography. For example, a change in sediment source position affects the extent and depth of sediments deposition in the simulation. Shifting the source point to the mid-section of the topography (the mid-point of the topography in a basin-ward direction) resulted in the accumulation of distal elements identical to turbidite lobe systems. This output is consistent with morphodynamic experiments by de Leeuw et al. (2016), where sediment discharge from the basin slope leads to the build-up of basin floor fan units.

Property Classification in Stratigraphic Model

In our opinion, the most appropriate output is the stratigraphic model in **Figure 5d**. This point of view is because, compared to the depositional description in studies such as Folkestad and Satur (2006); Kieft et al. (2011), and the seismic interpretation presents a similar stratigraphic sequence. Sediment distribution in each time step of the simulation was stacked into a single zone framework to attain a simplified model. This strategy assumes that sedimentary processes that lead to the final build-up of genetic related units within zones of the model will not vary significantly over the simulation period. The stratigraphic model (**Figure 5d**) was converted into a 3-D format (20 m x 20 m x 2 m grid cells) for the property modeling in PetrelTM.

Facies, porosity, and permeability representation in the stratigraphic model was done via a rule based approach in PetrelTM (see **Table 3**). The classification is driven by depositional depth, geologic flow velocity, and sediment distribution patterns as indicated in **Figure 7**. Lithofacies representation in the stratigraphic model relied on the sediment grain size pattern and proximity to sediment source. For example, shoreface lithofacies units are medium-to-coarse grained sediments, which accumulate at a proximal distance to the sediment source. In contrast, mudstone units are confined to fine-grained sediments in the distal section of the simulation domain.

Using knowledge from published studies by Kieft et al. (2011) and wireline-log attributes such as gamma ray, neutron, sonic, and density logs, porosity and permeability variations in the stratigraphic model are estimated (Table 1). In previous studies on the Sleipner Øst, and Volve field (Equinor, 2006; Kieft et al. 2011), shoreface deposits make up the best reservoir units, while lagoonal deposits formed the worst reservoir units. With this guide, shoreface sandstone units and mudstone/shale units in the forward stratigraphic model are best and worst reservoir units respectively. The porosity and permeability values in Table 4 are from equations in Statoil's petrophysical report of the Volve field (Equinor, 2016):

$$\varnothing_{er} = \varnothing_D + \alpha \cdot (NPHI - \varnothing_D) + \beta \quad (14)$$

where \varnothing_{er} is the estimated porosity range, \varnothing_D is density porosity, α and β are regression constants; ranging between -0.02 – 0.01 and 0.28 – 0.4 respectively, $NPHI$ is neutron porosity. In instances where $NPHI$ values for lithofacies units is not available from the published references, an average of 0.25 was used.

$$KLOGH_{er} = 10^{(2 + 8 \cdot PHIF - 5 \cdot VSH)} \quad (15)$$

where $KLOGH_{er}$ is the estimated permeability range, VSH is the volume of clay/shale in the lithofacies unit, and $PHIF$, the fractured porosity. The VSH range between 0.01 – 0.12 for the shoreface units, and 0.78 – 0.88 for lagoonal deposits.

Property Modeling in Petrel™

The workflow (**Figure 2b**) used for subsurface property modeling in Petrel™ is applied to represent lithofacies, porosity, and permeability properties in the stratigraphic model. These processes involve:

- (1) Structure modeling: identified faults within the study area are modeled together with interpreted surfaces from seismic and well correlation to generate the main structural framework, within which the property model is built. Here, fault pillars and connecting fault bodies are linked to obtain the kind of fault framework interpreted from the seismic data.
- (2) Pillar gridding: building a “grid skeleton” made up of a top, middle and base architectures. Typically, pillars join corresponding corners of every grid cell of the adjacent grid to form the

foundation for each cell within the model. The prominent orientation of faults (I-direction) within the model area was in an N-S and NE-SW direction, so the “I-direction” was set to NNE-SSW to capture the general structural description of the area.

(3) Horizons, Zones, and Vertical Layering: stratigraphic horizons and subdivisions (zones) delineate the geological formation’s boundaries. As stratigraphic horizons are introduced into the model grid, the surfaces are trimmed iteratively and modified along faults to correspond with displacements across multiple faults. Vertical layering shows the thicknesses and orientation between the layers of the model. Layers refers to significant changes in particle size or sediment composition in a geological formation. Using a vertical layering scheme makes it possible to honor the fault framework, pillar grid, and horizons. A constant cell thickness of 1 m is used in the model to control the vertical scale of lithofacies, porosity, and permeability modeling.

(4) Upscaling: involves the substitution of smaller grid cells with coarser grid cells. Here, log data is transformed from 1-dimensional to a 3-dimensional framework to evaluate which discrete value suits selected data point in the model. One advantage of the upscaling procedure is to make the modeling process faster.

Porosity and Permeability Modeling

The Volve field porosity and permeability model from Equinor are adopted as the base (reference) model. The model, which covers 17.9 km² was generated with the reservoir management software (RMS), developed by Irap and Roxar (EmersonTM). The petrophysical model has a grid dimension of 108 m x 100 m x 63 m and was compressed by 75.27% of cell size from an approximated cell size of 143 m x 133 m x 84 m. To achieve a comparable model resolution as the Volve field porosity and permeability model, the forward stratigraphic output, which had an initial resolution of 90 m x 78 m x 45 m, is upscaled to a grid of 107 m x 99 m x 63 m. Variograms being a critical aspect of this work, we submit two options to extrapolate variogram parameters from the forward stratigraphic-based porosity and permeability models. In Option 1, the porosity and permeability values were assigned to the synthetic lithofacies wells that correlate with known facies-association in the study area (see **Table 4**).

321 The pseudo wells comprising porosity and permeability are situated in-between well locations to guide
322 porosity and permeability simulation in the model. For option 2, the best-fit forward stratigraphic model
323 changes by assigning porosity and permeability attribute using the general stratigraphic orientation
324 captured in the seismic data (NE-SW; 240°). Porosity and permeability pseudo (synthetic) logs were then
325 extracted from the forward stratigraphic output to build the porosity and permeability models (**Figure 8**).
326 Porosity modeling is through normal distribution, while the permeability models were produced using a
327 log-normal distribution and the corresponding porosity property for collocated co-kriging.

328 Considering that vertical trends in options 1 and 2 will be similar within a sampled interval, option 2
329 presented a viable 3-D representation of property variations in the major and minor directions of the
330 forward stratigraphic model. Ten synthetic wells (SW), ranging between 80 m and 120 m in total depth
331 (TD), are positioned in the forward model to capture the vertical distribution of porosity-permeability at
332 different sections of the forward stratigraphic-based models.

333 The synthetic wells (**Figure 9 c**) with porosity and permeability data were upscaled, and distributed into
334 the original structural model using the sequential Gaussian simulation method. The synthetic wells
335 derived from the stratigraphic model served as an additional control for porosity and permeability
336 modeling in the Volve field. Because the variogram-based modeling approach is efficient in subsurface
337 data conditioning, this idea presents an opportunity to get more wells at no additional cost to control
338 porosity and permeability distribution. The variogram model (**Figure 10**) of dominant lithofacies units in
339 the stratigraphic model served as a guide in estimating variogram parameters for porosity and
340 permeability modeling. The variogram has major and minor range of 1400 m and 400 m respectively, and
341 an average sill value of 0.75. Six out of fifty model realizations that show some similarity to the original
342 porosity and permeability model formed the basis of our analysis (**Figure 11**). The selection of six
343 realizations was on a visual and statistical comparison of zones in the original Volve field model and the
344 stratigraphic-based porosity/permeability model. The statistical approach involved summary statistics
345 from the reference model and the stratigraphic-based porosity/permeability model. In contrast, the visual
346 evaluation compared the geological realism of forward stratigraphic-based realizations to the base model.

347 **Results**

348 The stratigraphic model in stage 4 (**Figure 5d iv**) shows the final geometry after 700,000 years of
349 simulation time. The initial stratigraphic simulation produced a progradation sequence with foreset-like
350 features (**Figure 5d i**) and a sequence boundary, which separates the initial simulated output from the
351 next prograding phase (**Figure 5d ii**). An aggradational stacking pattern commences and becomes
352 prominent in stage 3 (**Figure 5d iii**). These aggradational sequences observed in the forward stratigraphic
353 model are consistent with natural events where sediment supply matchup with accommodation due to
354 sea-level rise within a geological period (Muto and Steel, 2000; Neal and Abreu, 2009).

355 Impact of the forward stratigraphic simulation on porosity and permeability representation in the reservoir
356 model is evident by comparing its outcomes to the Volve field porosity and permeability models by using
357 two synthetic well (VP1 and VP2); sampled at a 5 m vertical interval. Taking into account the fact that
358 the Volve field petrophysical model (**Figure 11a**) went through various phases of history matching to
359 obtain a model to improve well planning and production strategies, it is reasonable to assume that porosity
360 and permeability distribution in the petrophysical model will be geologically realistic and less uncertain.
361 This view formed the basis for using the porosity and permeability models developed by Equinor as a
362 reference for comparing outputs in the stratigraphic model. **Table 5a** shows an almost good match in
363 porosity at different intervals in the forward stratigraphic-based models (i.e. R14, R20, R26, R36, R45,
364 and R49). An analysis of the well logs in the model area shows that a large proportion of reservoir porosity
365 is between 0.18 – 0.24. Also, the analysis of the forward stratigraphic-based porosity model is consistent
366 with the porosity range in the Volve field model (see Figure 12).

367 A notable limitation with this approach is the assumption that variogram parameters and stratigraphic
368 inclination within zones remained constant throughout the simulation. The difference in permeability
369 attributes between the original permeability model and the forward stratigraphic-based type is the
370 application of other measured parameters in the original model (**Table 5b**). Typically, a petrophysical
371 model like the Sleipner Øst and Volve field model will factor in other datasets such as special core analysis
372 (SCAL) and level of cementation, which enhances reservoir petrophysics assessment. Bearing in mind

that the forward stratigraphic model did not involve some of this additional information from the reservoir, it is practicable to suggest that results obtained in the forward stratigraphic-based porosity and permeability models have adequately conditioned to known subsurface data.

Discussion

Results show the influence of sediment transport rate (or diffusion rate), initial basin topography, and sediment source location on the stratigraphic simulation in GPMTM. Compared to studies such as Muto & Steel (2000) and Neal & Abreu (2009), we observed that a variation in sea-level controls the volume of sediment that is retained or transported further into the basin, therefore controlling the resultant stratigraphic sequences. In related work, Burges et al. (2008) suggest that a sediment-wedge topset width connects directly to the initial bathymetry, in which the sediment-wedge structure develops, and the correlation between sediment supply and accommodation rate. This opinion is in line with observations in this study, where the initial sediment deposit controls the geometry of subsequent phases of depositions in the hypothetical basin. The uncertainty of initial conditions used in this work led to the generation of multiple forward stratigraphic scenarios to account for the range of bathymetries that may have influenced sediment transportation to form the present-day reservoir units in the Volve field.

The simulation produced well-defined sloping depositional surfaces in a stratigraphic architecture (clinoforms) and sequence boundaries that depict patterns seen in the seismic data. In their work, Allen and Posamentier (1993); Ghandour and Haredy (2019) explained the importance of sequence stratigraphy in lithofacies characterization, and therefore petrophysical property distribution in sedimentary systems. Also, sediment deposition into a geological basin in the natural order is controlled by mechanical and geochemical processes that modify petrophysical attributes (Warrlich et al. 2010); therefore, using different geological processes and initial conditions to generate depositional scenarios in 3-dimension provides a framework to analyse property variations in a hydrocarbon reservoir. The approach produces a porosity-permeability model comparable to the original petrophysical model using synthetic porosity and permeability logs from the forward stratigraphic model as input datasets. As mentioned, this work did not include variations in the layering scheme that develops in different zones of the stratigraphic

399 model. Under this circumstance, there is a possibility to overestimate and or underestimate porosity and
400 permeability property in some sampled intervals in the validation wells. Therefore, we suggest that the
401 forward stratigraphic simulation outputs such as the example presented in this contribution serve as
402 additional data to understand sediment distribution patterns and associated vertical and horizontal
403 petrophysical trends in the depositional environment, and not as absolute conditioning data in subsurface
404 property modeling.

405 The assumptions made concerning the type of geological processes and input parameters in the
406 stratigraphic simulation certainly differ from what existed during sediment deposition. So, applying
407 stratigraphic models that fit a basin-scale description to a relatively smaller scale reservoir presents
408 another level of uncertainty in the approach. This finding agrees with Burges et al., (2008), where they
409 indicate that the diffusion geological process simulation fits the description of large-scale sediment
410 transportation. This view further buttresses the point that integrating forward stratigraphic simulation into
411 a well-scale framework has a high chance of producing outcomes that deviate from the real-world
412 subsurface description. In line with observations in Bertonecello et al. (2013); Aas et al. (2014); and Huang
413 et al. (2015) in relations to limitations in the forward stratigraphic simulation method, it is advisable to
414 use its outputs cautiously in reservoir modeling; as such outputs from forward stratigraphic models could
415 lead to an increase in property representation bias in a model.

416 The correlation between reservoir lithofacies and petrophysics, and its prediction through reservoir
417 models, have been extensively examined in several studies (Falivene et al.,2006; Hu and
418 Chugunova,2008). Meanwhile, the predicted outputs most often do not depict the actual reservoir
419 character due to the absence of a realistic 3-D stratigraphic framework to guide reservoir property
420 representation in geological models. The forward stratigraphic modeling method, notwithstanding its
421 limitations, provides reservoir modeling practitioners an platform to generate subsurface models that
422 reflect the natural variation of reservoir properties.

Conclusion

In this paper, variogram parameters from a forward stratigraphic simulation are combined with subsurface data to constrain porosity and permeability distribution in the Volve field model. The caution for subsurface modeling practitioners is that the stratigraphic simulation scenarios presented in this contribution do not prove that spatial and geometrical data derived from forward stratigraphic models are absolute input parameters for a real-world reservoir modeling task. Uncertainties in the choice of boundary conditions and processes for the stratigraphic simulation led the variation of input parameters to attain a depositional architecture that is geologically realistic and comparable to the stratigraphic correlation suggested in some published studies of the study area. The match in porosity obtained by comparing validation wells in the original and stratigraphic-based petrophysical model indicates that combining variogram parameters from well data and forward stratigraphic simulation outputs will improve property prediction in inter-well zones. This suggestion supports the idea that more conditioning data (well data) will increase the chance of producing realistic property distribution in the model area. This work also made some key findings:

1. For specific stratigraphic simulation in GPMTM and a range of model parameters, sediment transportation and deposition is based on diffusion rate and proximity to sediment source. This opinion is consistent with several published works on sequence stratigraphy and or system tracts in shallow marine settings. However, further work with different stratigraphic modeling simulators could mitigate some of the challenges faced in this work.
2. A lithofacies distribution that is consistent with previous studies was produced in the stratigraphic model. This position is evident in scenarios where sediment distribution vertically matches with lithofacies variation in a sampled interval in an actual well log.

Geologically feasible stratigraphic patterns generated in the forward stratigraphic model provide additional confidence in the representation of lithofacies, and therefore porosity and permeability property variations in the depositional setting under study. The resultant forward stratigraphic-based porosity and permeability model suggests that forward stratigraphic simulation outputs can be

449 integrated into classical modeling workflows to improve subsurface property modeling and well
450 planning strategies.

451 **Data and Code Availability**

452 The datasets for this work are from Equinor on their operations in Volve field, Norway. The data include
453 24 suits of well logs, and 3-D reservoir models in Eclipse and RMS formats. The data, models (eclipse and
454 RMS formats), and the rule-based calculation script to generate lithofacies and porosity/permeability proportions
455 are archived on Zenodo as Otoo & Hodgetts, (2020).

456 **GPM™ Software**

457 The (2019.1) version of GPM™ software was used in completing this work after an initial 2018.1 version. Available
458 on: <https://www.software.slb.com/products/gpm>. The software license and code used in the GPM™ cannot be
459 provided, because Schlumberger does not allow the code for its software to be shared in publications.

460 **Model Availability in Petrel™**

461 The work started in Petrel™ software (2017.1), but it was completed with Petrel™ software (2019.1).
462 The software is available on: <https://www.software.slb.com/products/petrel>. The software runs on a
463 Windows PC with the following specifications: Processor; Intel Xeon CPU E5-1620 v3 @3.5GHz 4
464 cores-8 threads, Memory; 64 GB RAM. The computer should be high end, because a lot of processing
465 time is required for the task. The forward stratigraphic models are in Zenodo as Otoo & Hodgetts, (2020).

466 **Author Contribution**

467 Daniel Otoo designed the model workflow, conducted the simulation using the GPM™ software, and
468 evaluated the results. David Hodgetts converted the Volve field data into Petrel compactible format for
469 easy integration with outputs from the forward stratigraphic simulation.

470 **Acknowledgement**

471 Thanks to Equinor for making available the Volve field dataset. Also, thanks to Schlumberger for
472 providing us with the GPM™ software license. A special thanks to Mostfa Legri (Schlumberger) for his
473 technical support in the use of GPM™. Finally, to the Ghana National Petroleum Corporation (GNPC)
474 for sponsoring this research.

475 **References**

- 476 Aas, T., Basani, R., Howell, J. & Hansen, E.: Forward modeling as a method for predicting the distribution of deep-
477 marine sands: an example from the Peira Cava sub-basin. *The geologic society*, 387(1), 247-269,
478 doi:10.1144/SP387.9, 2014.
- 479 Allen, G. P. and Posamentier, H. W.: Sequence stratigraphy and facies model of an incised valley fill; the Gironde
480 Estuary, France. *Journal of Sedimentary Research*; 63 (3), 378–391, doi:/10.1306/D4267B09-2B26-11D7-
481 8648000102C1865D, 1993.
- 482 Bajpai, V.N., Saha Soy, T.K., Tandon, S.K.: Subsurface sediment accumulation patterns and their relationships
483 with tectonic lineaments in the semi-arid Luni river basin, Rajasthan, Western India. *Journal of Arid Environments*,
484 48(4); 603-621, 2001.
- 485 Bertoncello, A., Sun, T., Li, H., Mariethoz, G., & Caers, J.: Conditioning Surface-Based Geological Models to
486 Well and Thickness Data. *International Association of Mathematical Geoscience*, 45, 873-893, doi:
487 10.1007/s11004-013-9455-4, 2013.
- 488 Burges, P.M., Steel, R.J., & Granjeon, D.: Stratigraphic Forward Modeling of Basin-Margin Clinoform Systems:
489 Implications for Controls on Topset and Shelf Width and Timing of Formation of Shelf-Edge deltas. Recent
490 advances in models of siliciclastic shallow-marine stratigraphy. *SEPM (Society for Sedimentary Geology) Special*
491 Publication, vol. 90, SEPM (Society for Sedimentary Geology), 35-45, 2008.
- 492 Caers, J., & Zhang, T.: Multiple-point geostatistics: a quantitative vehicle for integrating geologic analogs into
493 multiple reservoir models, in Grammer, G. M., Harris, P. M., and Eberli, G. P., eds., *Integration of outcrop and*
494 *modern analogs in reservoir modeling*. Am. Assoc. Petrol. Geol. Memoir, 384–394, 2004.
- 495 Cheng, F., Garzione, C., Jolivet, M., Guo, Z., Zhang, D., & Zhang, C.: A New Sediment Accumulation Model of
496 Cenozoic Depositional Ages From the Qaidam Basin, Tibetan Plateau. *Journal of Geophysical Research; Earth*
497 *Surface*. 123, 3101-3121, 2018
- 498 Cockings, J.H., Kessler, L.G., Mazza, T.A., & Riley, L.A.: Bathonian to mid-Oxfordian Sequence Stratigraphy of
499 the South Viking Graben, North Sea. *Geological Society, London, Special publications*, 67, 65–105,
500 doi:10.1144/GSL.SP.1992.067.01.04, 1992.
- 501 Dade, W.B. & Friend, P.F.: Grain Size, Sediment Transport Regime, and Channel Slope in Alluvial Rivers. *The*
502 *Journal of Geology*, 106(6), 661-676, 1998.
- 503 Dashtgard, S.E., White, R.O., Butler, K.E., Gingras, M.: Effects of relative sea level change on the depositional
504 character of an embayed beach, Bay of Fundy, Canada. *Marine Geology*, 239(3), 143-161, 2007.
- 505 Deutsch, C. & Journel, A.: GSLIB. Geostatistical software library and user's guide. *Geological magazine*, 136(1),
506 83-108, doi:10.2307/1270548, 1999.

De Leeuw, J., Eggenhuisen, J.T., & Cartigny, M.J.B.: Morphodynamics of submarine channel inception revealed by new experimental approach. *Nature Communication*, 7, 10886, 2016.

Dubrule, O.: *Geostatistics in Petroleum Geology*. American Association of Petroleum Geologist, 38, 27-101, doi:10.1306/CE3823, 1998.

Falivene, O., Arbues, P., Gardiner, A., & Pickup, G.E.: Best practice stochastic facies modeling from a channel-fill turbidite sandstone analog (the Quarry outcrop, Eocene Ainsa basin, northeast Spain. *American Association of Petroleum Geologist*, 90(7), 1003-1029, doi:10.1306/02070605112, 2006.

Folkestad, A., & Satur, N.: Regressive and transgressive cycles in a rift-basin: Depositional model and sedimentary partitioning of the Middle Jurassic Hugin Formation, Southern Viking Graben, North Sea. *Sedimentary Geology*. 207, 1-21, doi:10.1016/j.sedgeo.2008.03.006, 2008.

Ghandour, I.M. and Haredy, R.A.: *Facies Analysis and Sequence Stratigraphy of Al-Kharrar Lagoon Coastal Sediments, Rabigh Area, Saudi Arabia: Impact of Sea-Level and Climate Changes on Coastal Evolution*. *Arabian Journal for Science and Engineering*, 44(1), 505-520, 2019.

Harbaugh, J.W.: *Simulating Sedimentary Basins: An Overview of the SEDSIM Model and its Relevance to Sequence Stratigraphy*. *Geoinformatics*, 4(3), 123-126, 1993.

Hassanpour, M., Pyrcz, M. & Deutsch, C.: Improved geostatistical models of inclined heterolithic strata for McMurray formation, Canada. *AAPG Bulletin*, 97(7), 1209-1224, doi:10.1306/01021312054, 2013.

Hodgetts, D.D., Drinkwater, N.D., Hodgson, J., Kavanagh, J., Flint, S.S., Keogh, K.J. and Howell, J.A.: Three-dimensional geological models from outcrop data using digital data collection techniques: an example from the Tanqua Karoo depocenter, South Africa. *Geological Society, London*, v. 171 (4), 57–75, doi:10.1144/GSL.SP.2004.239.01.05, 2004.

Hu, L.Y., and Chugunova, T.: Multiple-point geostatistics for modeling subsurface heterogeneity: A comprehensive review. *Water Resource Research*, 44 (11), 1-14, doi:10.1029/2008WR006993, 2008.

Huang, X., Griffiths, C. & Liu, J.: Recent development in stratigraphic forward modeling and its application in petroleum exploration. *Australian journal of Earth science*, 62(8), 903-919, doi:10.1080/081200991125389, 2015.

Husmo, T. & Hamar, G.P. & Høiland, O. & Johannessen, E.P. & Rømuld, A. & Spencer, A.M. & Titterton, Rosemary.: Lower and Middle Jurassic. In: *The Millennium Atlas: Petroleum Geology of the Central and Northern North Sea*, 129-155, 2003.

Kelkar, M., & Perez, G.: *Applied Geostatistics for Reservoir Characterization*. Society of Petroleum Engineers. [https://www.academia.edu/36293900/Applied Geostatistics for Reservoir characterization](https://www.academia.edu/36293900/Applied_Geostatistics_for_Reservoir_characterization). Accessed 10 September, 2019, 2002.

Kieft, R.L., Jackson, C.A.-L., Hampson, G.J., and Larsen, E.: Sedimentology and sequence stratigraphy of the Hugin Formation, Quadrant 15, Norwegian sector, South Viking Graben. *Geology Society, London, Petroleum Geology Conference Series*, 7, 157-176, doi:10.1144/0070157, 2011.

541 Milner, P.S., and Olsen, T.: Predicted distribution of the Hugin Formation reservoir interval in the Sleipner Øst
542 field, South Viking Graben; the testing of a three-dimensional sequence stratigraphic model. In: Gradstein, F.M.,
543 Sandvik, K.O., Milton, N.J. (Eds.), Sequence Stratigraphy; Concepts and Applications. Special Publication, Vol 8.
544 Norwegian Petroleum Society, 337-354, 1998.

545 Muto, T., and Steel, R.J.: The accommodation concept in sequence stratigraphy: Some dimensional problems and
546 possible redefinition. *Geology*, 130(1), 1-10, 2000.

547 Neal, J., and Abreu, V.: Sequence stratigraphy hierarchy and the accommodation succession method. *Geology*,
548 37(9), 779-782, 2009.

549 Otoo, D., and Hodgetts, D.: Geological Process Simulation in 3-D Lithofacies Modeling: Application in a Basin
550 Floor Fan Setting. *Bulletin of Canadian Petroleum Geology*, 67(4), 255-272, 2019.

551 Otoo, D. & Hodgetts, D. Data citation for a forward stratigraphic-based porosity and permeability model developed
552 for the Volve field, Norway. Dataset. Zenodo. <http://doi.org/10.5281/zenodo.3855293>, 2020.

553 Orellana, N. Cavero, J. Yemez, I. Singh, V. and Sotomayor, J.: Influence of variograms in 3D reservoir-modeling
554 outcomes: An example. *The leading edge*, 33(8), 890-902, doi:10.1190/tle33080890.1, 2014.

555 Patruno, S., and Hansen, W.H.: Clinoforms and clinoform systems: Review and dynamic classification scheme for
556 shorelines, subaqueous deltas, shelf edges and continental margins. *Earth-Science Reviews*, 185, 202-233, 2018.

557 Ravasi, M., Vasconcelos, I., Curtis, A. and Kristi, A.: Vector-acoustic reverse time migration of Volve ocean-
558 bottom cable data set without up/down decomposed wavefields. *Geophysics* 80 (4): 137-150,
559 doi:10.1190/geo2014-0554.1, 2015.

560 Ringrose., P. & Bentley., M.: Reservoir model design: A practioner's guide. First edition ed. New York: Springer
561 business media B.V. 20-150, 2015.

562 Rijn, L.C., Walstra, D.J.R., Grasmeijer, B., Sutherland, J., Pan, S., & Sierra, J.P.: The predictability of cross-shore
563 bed evolution of sandy beaches at the time scale of storms and seasons using process-based profile models. *Coastal*
564 *engineering*, 47(3), 295-327, doi:10.1016/S0378-3839(02)00120-5, 2003.

565 Schlumberger™ Softwares.: Geological Process Modeling, Petrel™ version 2019.1, Schlumberger, Norway. URL:
566 <https://www.sdc.oilfield.slb.com/SIS/downloads.aspx>, 2019.

567 Sclater, J.G. & Christie, P.A.F.: Continental stretching: An explanation of the Post-Mid-Cretaceous subsidence of
568 the central North Sea Basin. *Journal of Geophysical Research, Solid Earth*; 85(7), 3711-3739, 1980.

569 Singh, V., & Yemez, I., & Sotomayor de la Serna, J.: Integrated 3D reservoir interpretation and modeling: Lessons
570 learned and proposed solutions. *The Leading Edge*. 32(11), 1340-1353, doi:10.1190/tle32111340.1, 2013.

571 Skalinski, M., & Kenter, J.: Carbonate petrophysical rock typing: Integrating geological attributes and
572 petrophysical properties while linking with dynamic behaviour. Geological Society, London, Special Publications.
573 406 (1), 229-259, 2014.

574 Sneider, J.S., de Clarens, P., and Vail, P.R.: Sequence stratigraphy of the Middle and Upper Jurassic, Viking
575 Graben, North Sea. In: Steel, R.J., Felt, V.L., Johannessen, E.P., Mathieu, C. (Eds.), Sequence Stratigraphy on the
576 Northwest European Margin. Special Publication, vol. 5. Norwegian Petroleum Society, 167–198,
577 doi:10.1016/S0928-8937(06)80068-8, 1995.

578 Statoil, “Sleipner Øst, Volve Model, Hugin and Skagerrak Formation Petrophysical Evaluation, 2006”,
579 Stavanger, Norway. Accessed on: April, 27, 2019. Online: [https://www.equinor.com/volve-field-data-village-](https://www.equinor.com/volve-field-data-village-download)
580 [download](https://www.equinor.com/volve-field-data-village-download).

581 Strebelle, S., & Levy, M.: Using multiple-point statistics to build geologically realistic reservoir models: the
582 MPS/FDM workflow. Geological Society London, special publication, 309, 67-74, doi:10.1144/SP309.5, 2008.

583 Tetzlaff, D.M. & Harbaugh, J.W.: Simulating Clastic Sedimentation. New York: Van Nostrand Reinhold, 1989.

584 Otoo, D. 2021: Conversation with Daniel Tetzlaff, 4 February.

585 Varadi, M., Antonsen, P., Eien, M., & Hager, K.: Jurassic genetic sequence stratigraphy of the Norwegian block
586 15/5 area, South Viking Graben. In: Gradstein, F. M., Sandvik, K.O., & Milton, N.J., (eds) Sequence Stratigraphy
587 – Concepts and Applications. Norwegian Petroleum Society, Trondheim, special publication, 373-401, 1998.

588 Vollset, J. and Dore, A.G.: A revised Triassic and Jurassic lithostratigraphic nomenclature for the Norwegian North
589 Sea. NPD Bulletin Oljedirektoratet, 3, 53, 1984.

590 Walter C. P.: Relationship between eustacy and stratigraphic sequences of passive margins. GSA Bulletin; 89 (9),
591 1389–1403, 1978.

592 Winterer, L. W., Bosellini, A.: Subsidence and Sedimentation on Jurassic Passive Continental Margin, Southern
593 Alps, Italy. AAPG Bulletin; 65 (3), 394–421, doi: 10.1306/2F9197E2-16CE-11D7-8645000102C1865D, 1981.

594 Warrlich, G., Hillgartner, H., Rameil, N., Gittins, J., Mahruqi, I., Johnson, T., Alexander, D., Wassing, B.,
595 Steenwinkel, M., & Droste, H.: Reservoir characterisation of data-poor fields with regional analogues: a case study
596 from the Lower Shuaiba in the Sultanate of Oman, p. 577, 2010.

597 Zhong, D.: Transport Equation for Suspended Sediments Based on Two-Fluid Model of Solid/Liquid Two-Phase
598 Flows. Journal of Hydraulic Engineering; 137(5), 530-542, doi: 10.1061/(ASCE)HY.1943-7900.0000331, 2011.

List of Figures

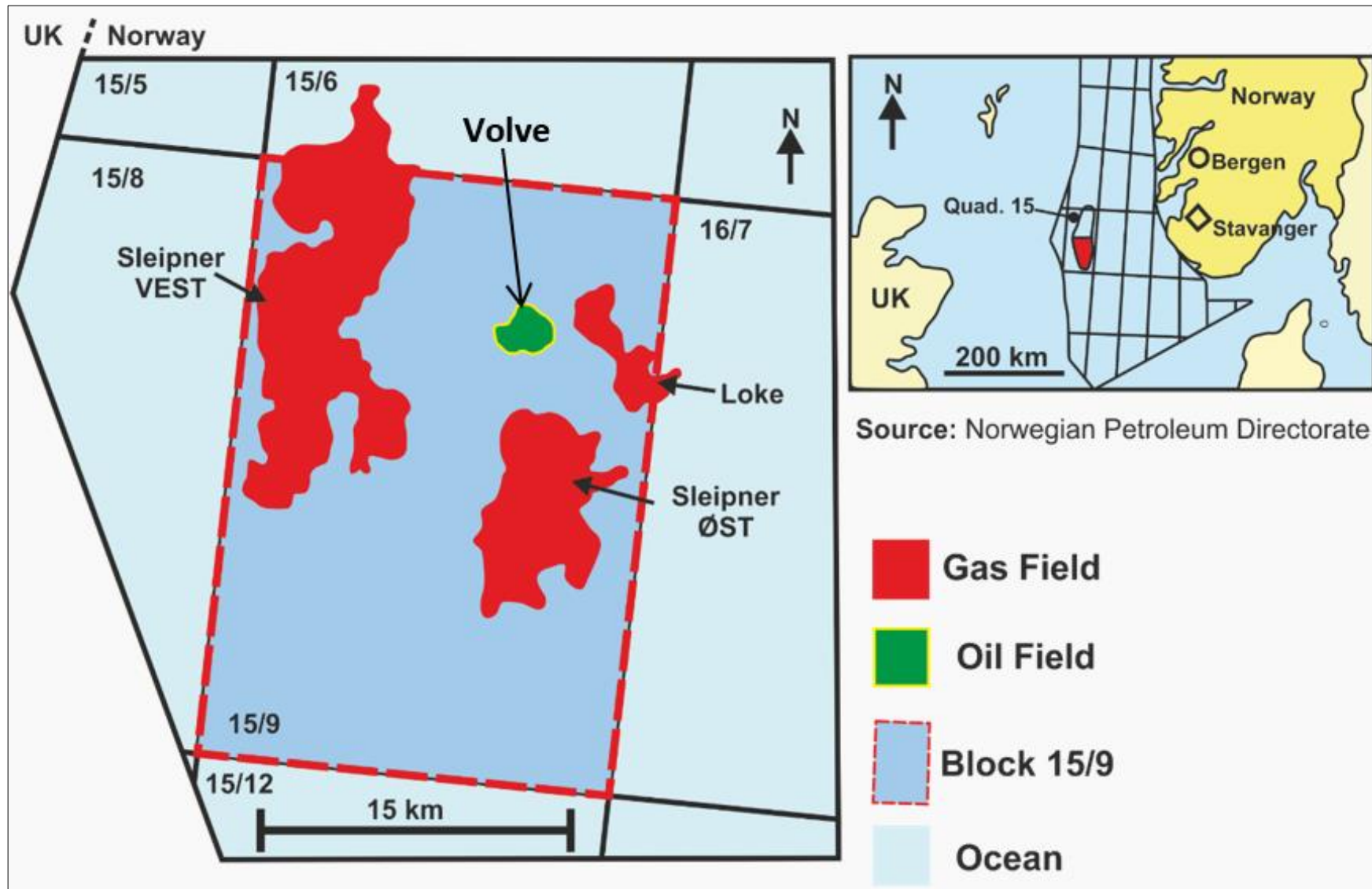


Fig 1. Location map of the Volve field; showing gas and oil fields in quadrant 15/9, Norwegian North Sea (from Ravasi et al., 2015).

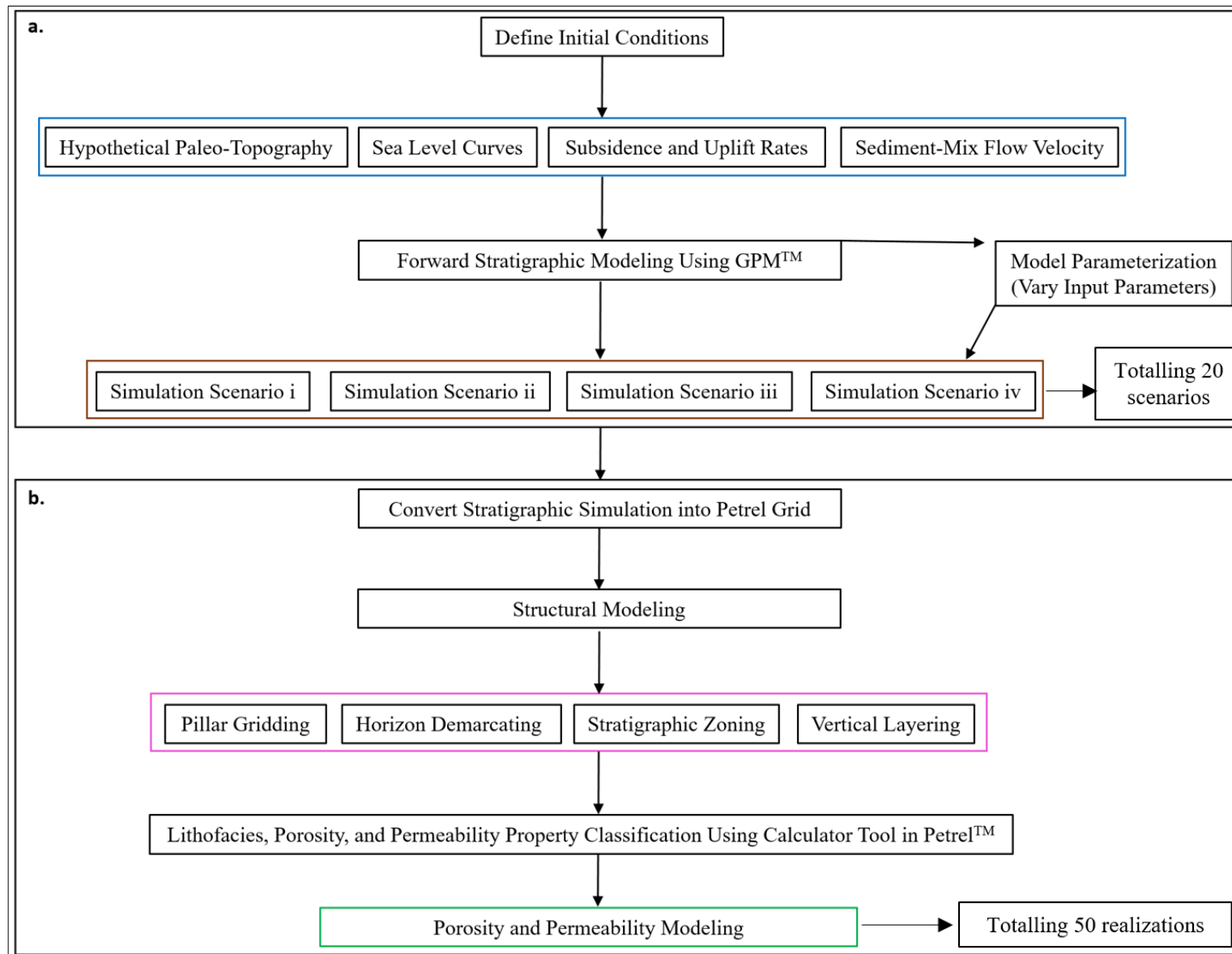


Fig 2. Schematic workflow of processes involved in this work. a. providing information of boundary conditions (input parameters) used in the forward stratigraphic simulation in GPM™; b. demonstrate how the forward stratigraphic model are converted into a grid that is usable in Petrel™ for porosity and permeability modeling.

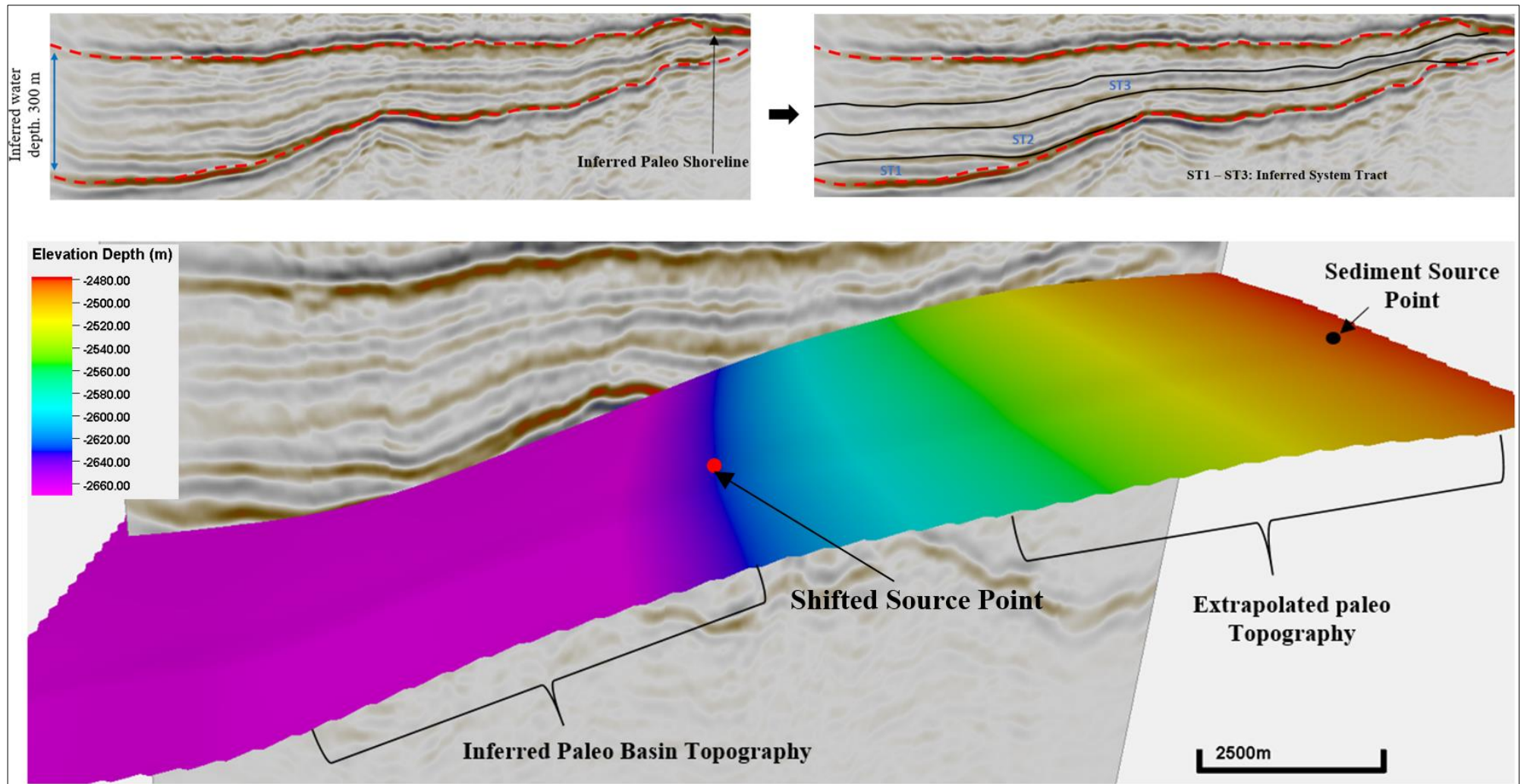


Fig 3. 3-D seismic section of the study area, from which the hypothetical topographic surface is derived for the simulation. The sedimentary entry point into the basin is located in the North Eastern section (based on Kieft et al. 2011).

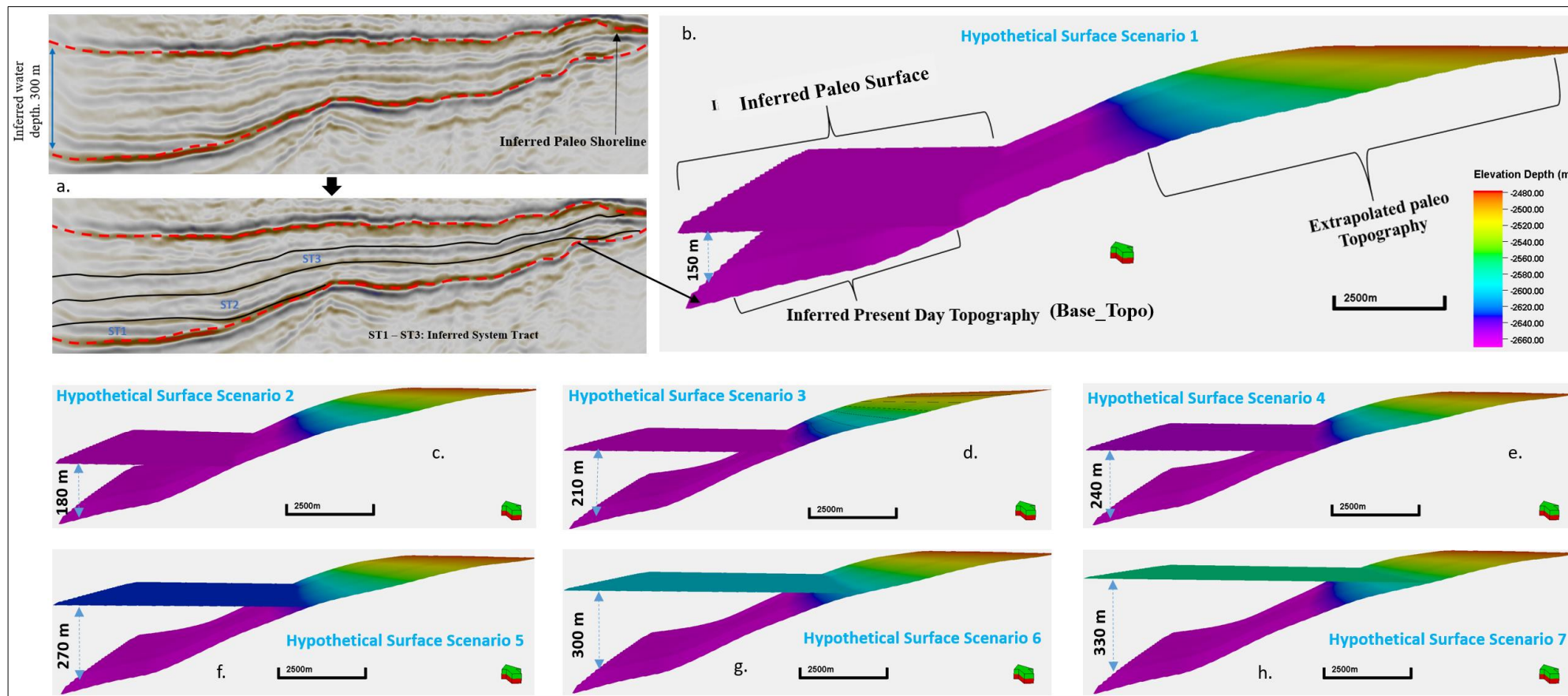


Fig 4. Paleo topographic surface from seismic. Also, illustrating different topographic surface scenarios that are produced for the simulation.

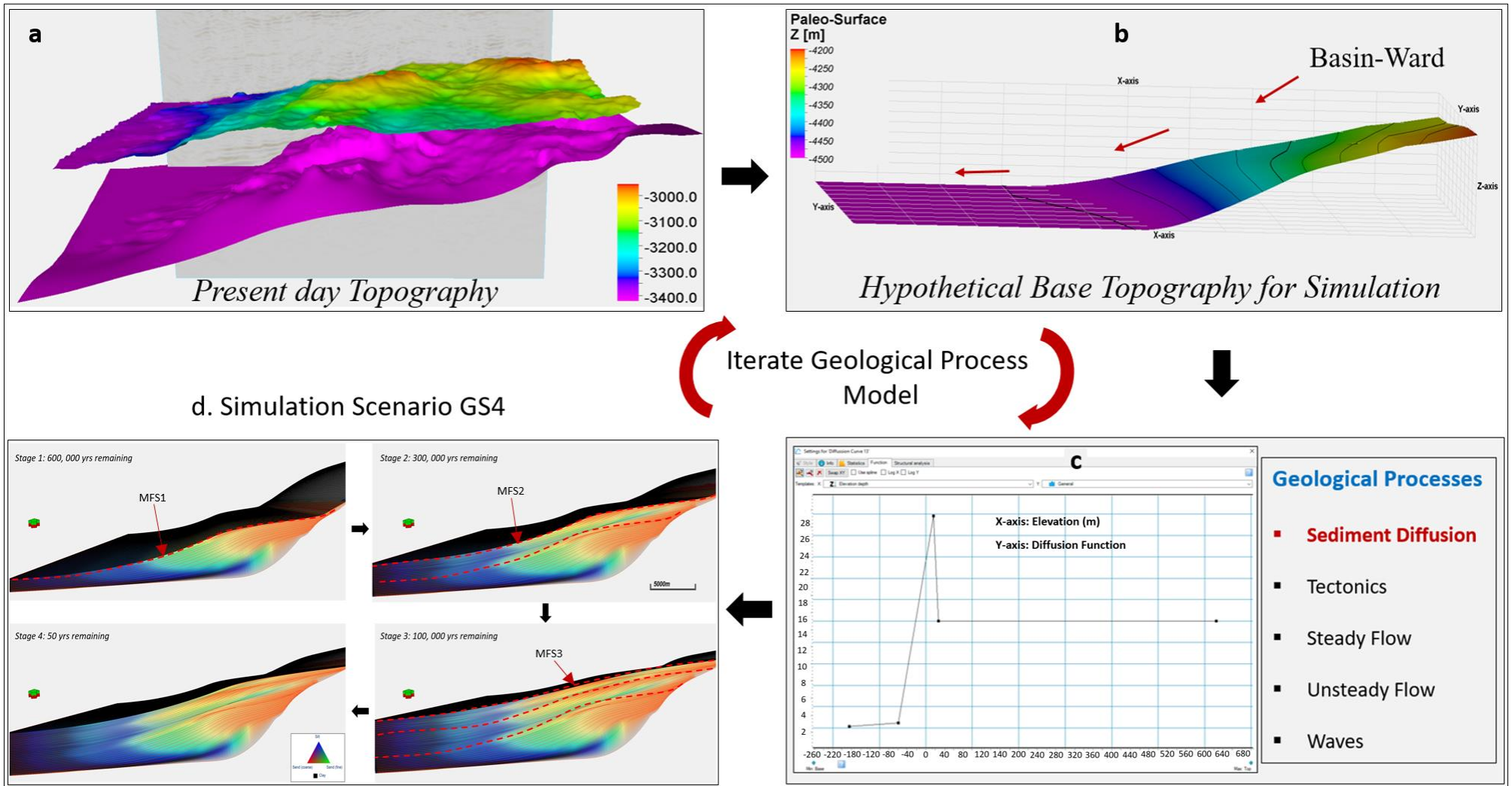


Fig 5. a. present-day top and bottom topographic surfaces of the Hugin formation; b. hypothetical topographic surface from seismic data; c. geological processes involved in the forward stratigraphic simulation; d. forward stratigraphic models at different simulation time intervals.

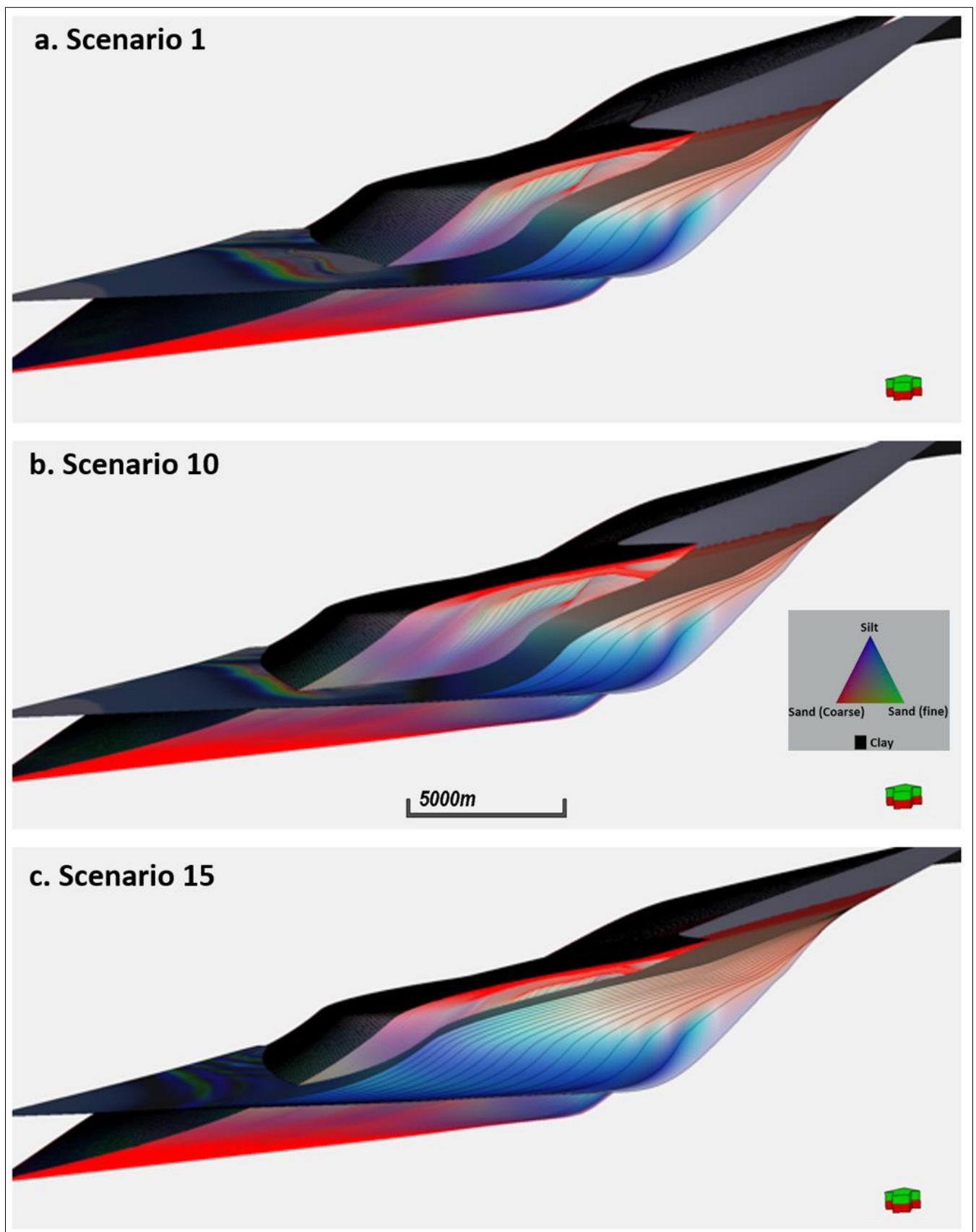


Fig 6. Stratigraphic simulation scenarios depicting sediment deposition in a shallow marine framework. **a.** scenario 1 involves equal proportions of sediment input, a relatively low subsidence rate and low water depth, **b.** scenario 10 uses high proportions of fine sand and silt (70%) in the sediment mix, abrupt changes in subsidence rate, and a relatively high water depth, **c.** scenario 15 involves very high proportions of fine sand and silt (80%), steady rate of subsidence and uplift in the sediment source area, and a relatively low water depth.

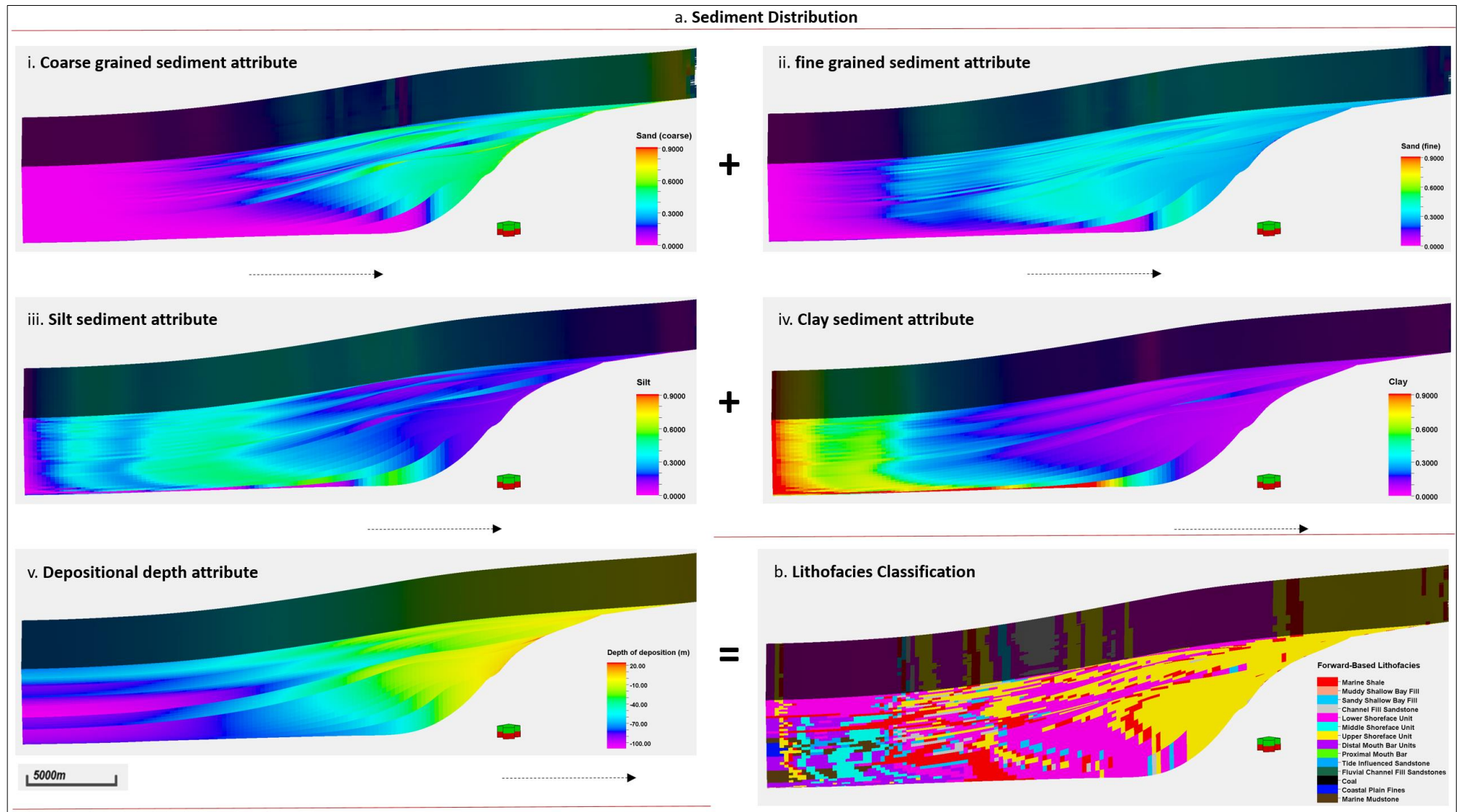


Fig 7 a. Sediment distribution patterns in the geological process modeling software. **b.** lithofacies classification using the property calculator tool in Petrel™.

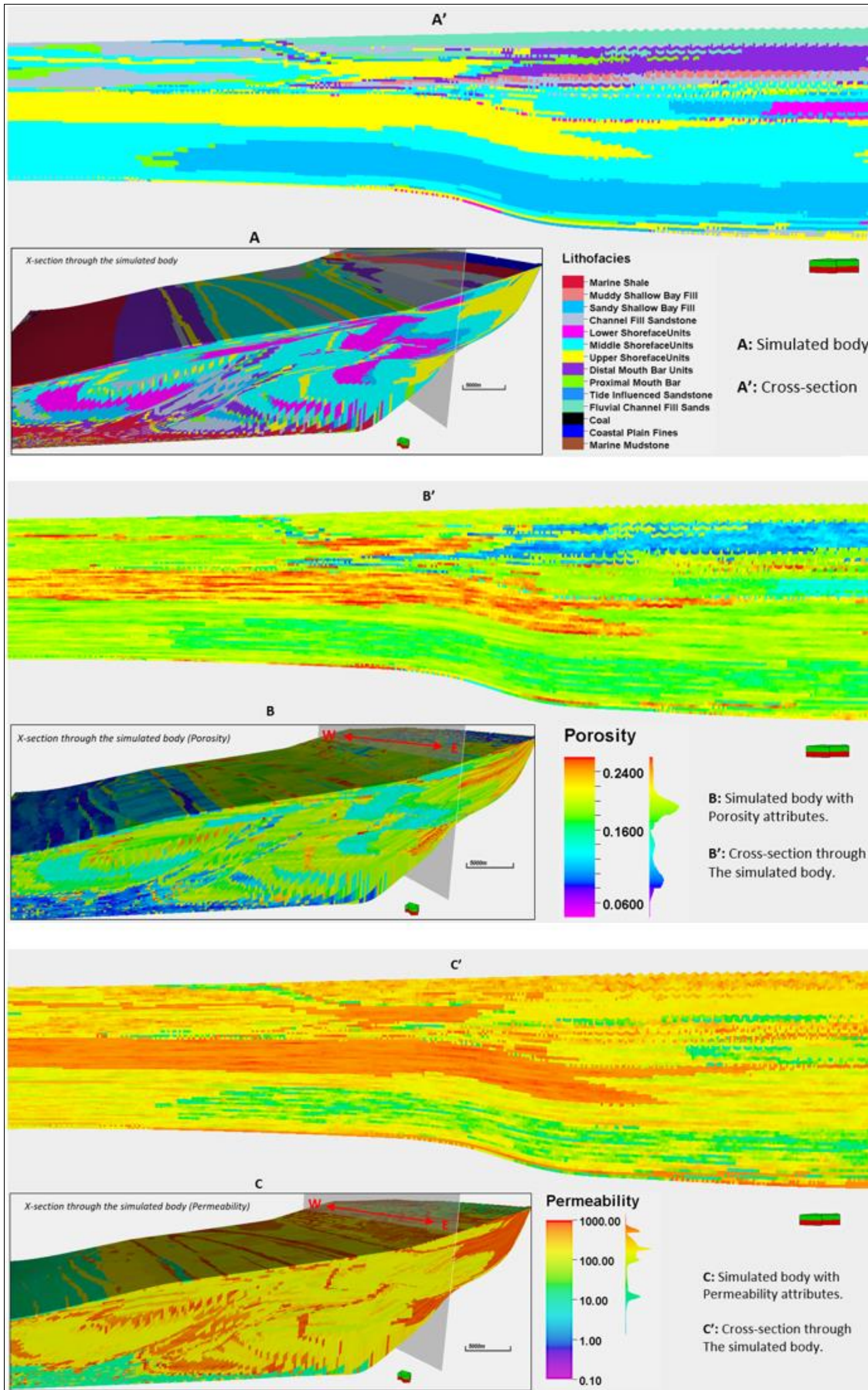


Fig 8. Lithofacies, porosity and permeability characterization in the stratigraphic model through the property calculator tool in Petrel™. Also, is a cross-sectional view of the 3-D models.

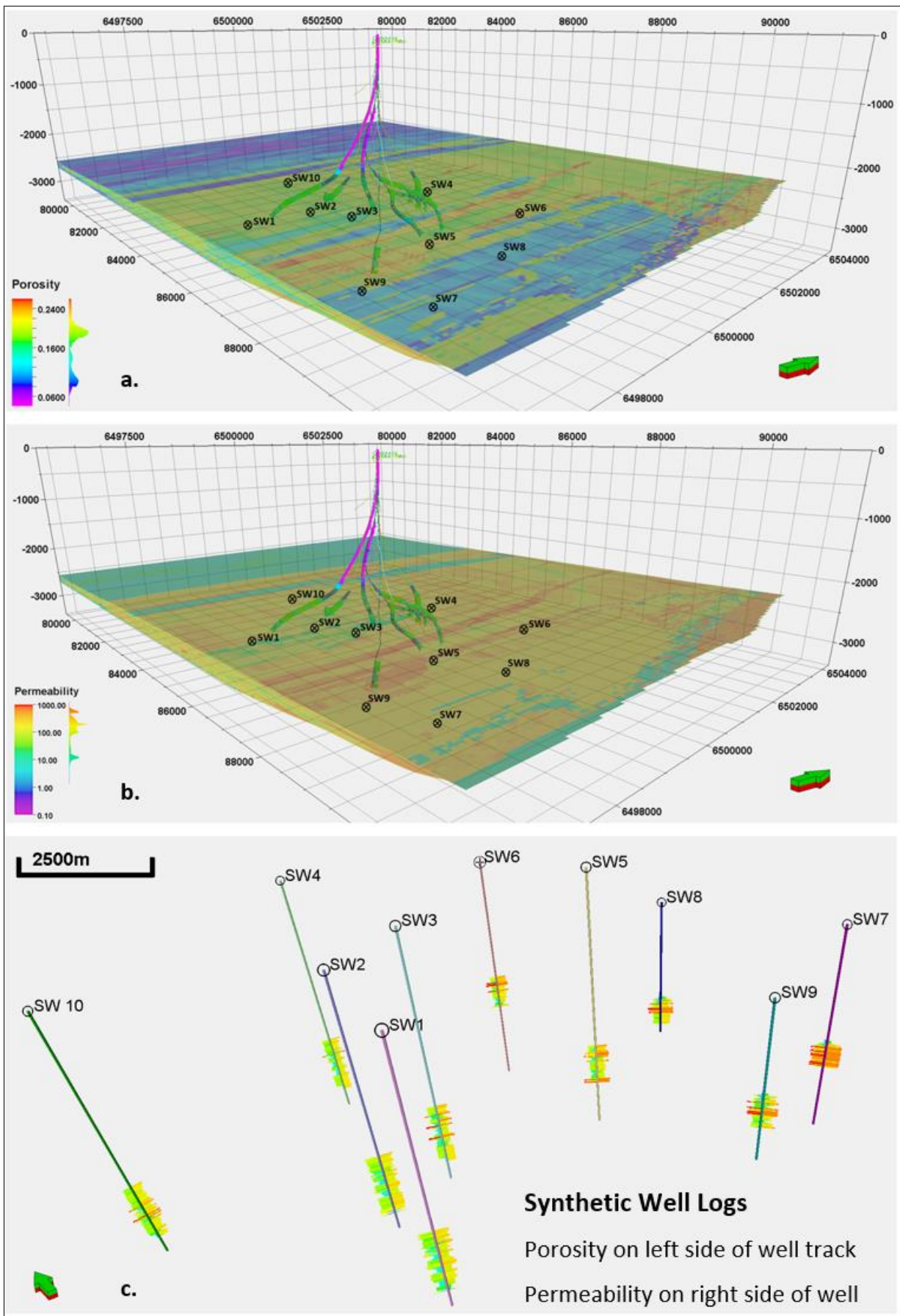


Fig 9. Synthetic wells from a forward stratigraphic-driven porosity and permeability model. The average separation distance between the synthetic wells shown in Figure 9c is about 0.9 km apart (maximum and minimum separation distance of 1.3 km and 0.65 km, respectively).

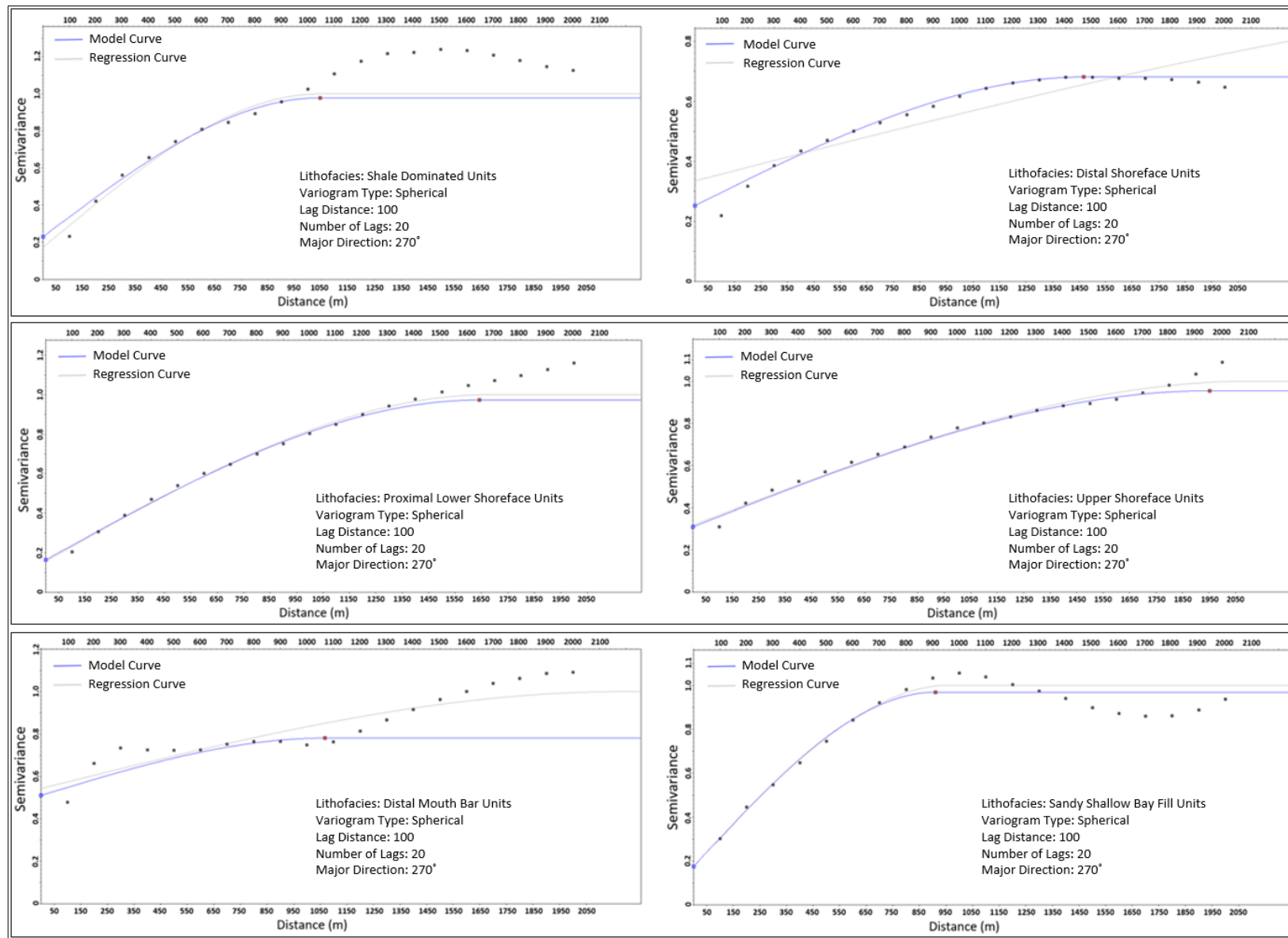


Fig 10. Variogram model of dominant lithofacies units from the forward stratigraphic model. The points indicate the number of lags in the variogram. The distance between these lags is about 100 m. This figure shows the lags between sample pairs for calculating the variogram in the major direction (NE-SW) of the stratigraphic model.

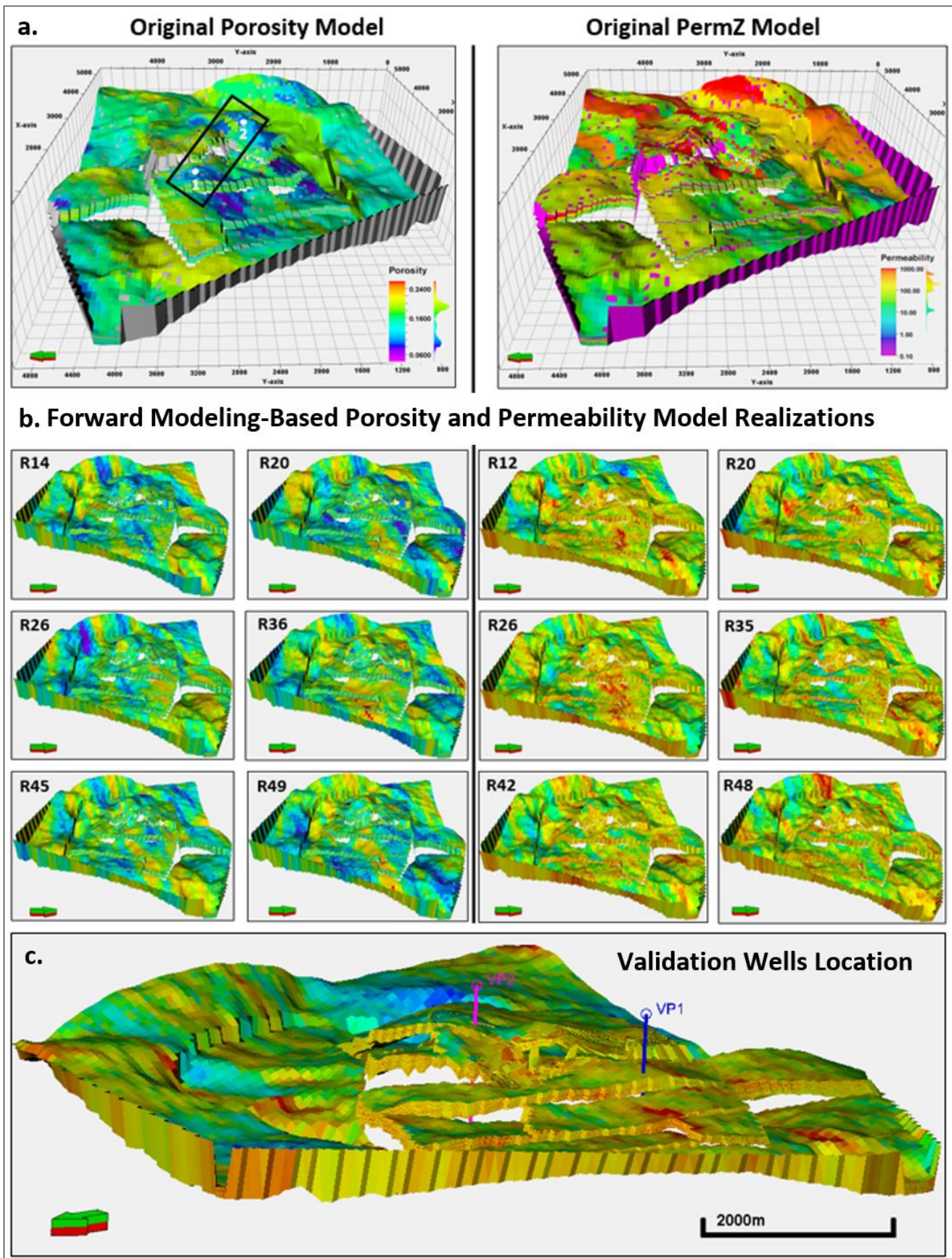


Fig 11. Original Volve field model vs the forward modeling-based models. Realizations 16, 20, 26, 36, 45, and 49 on the left half are porosity models, while realizations 12, 20, 26, 35, 42, and 48 on the right half are permeability models.

a. Validation Well 1

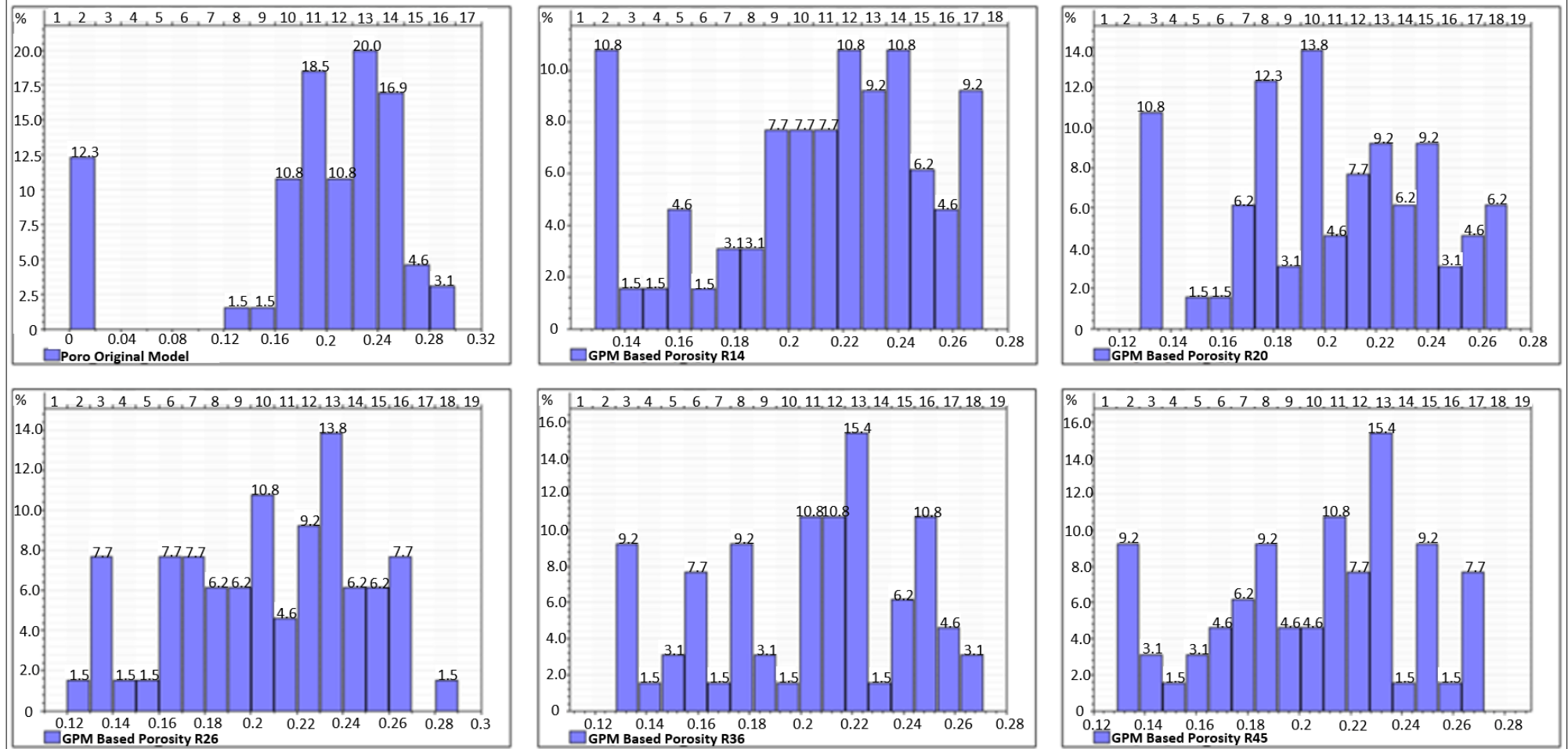


Figure 12a. Comparing porosity in validation Well 1 in five stratigraphic-based realizations, and the original model at similar vertical intervals.

b. Validation Well 2

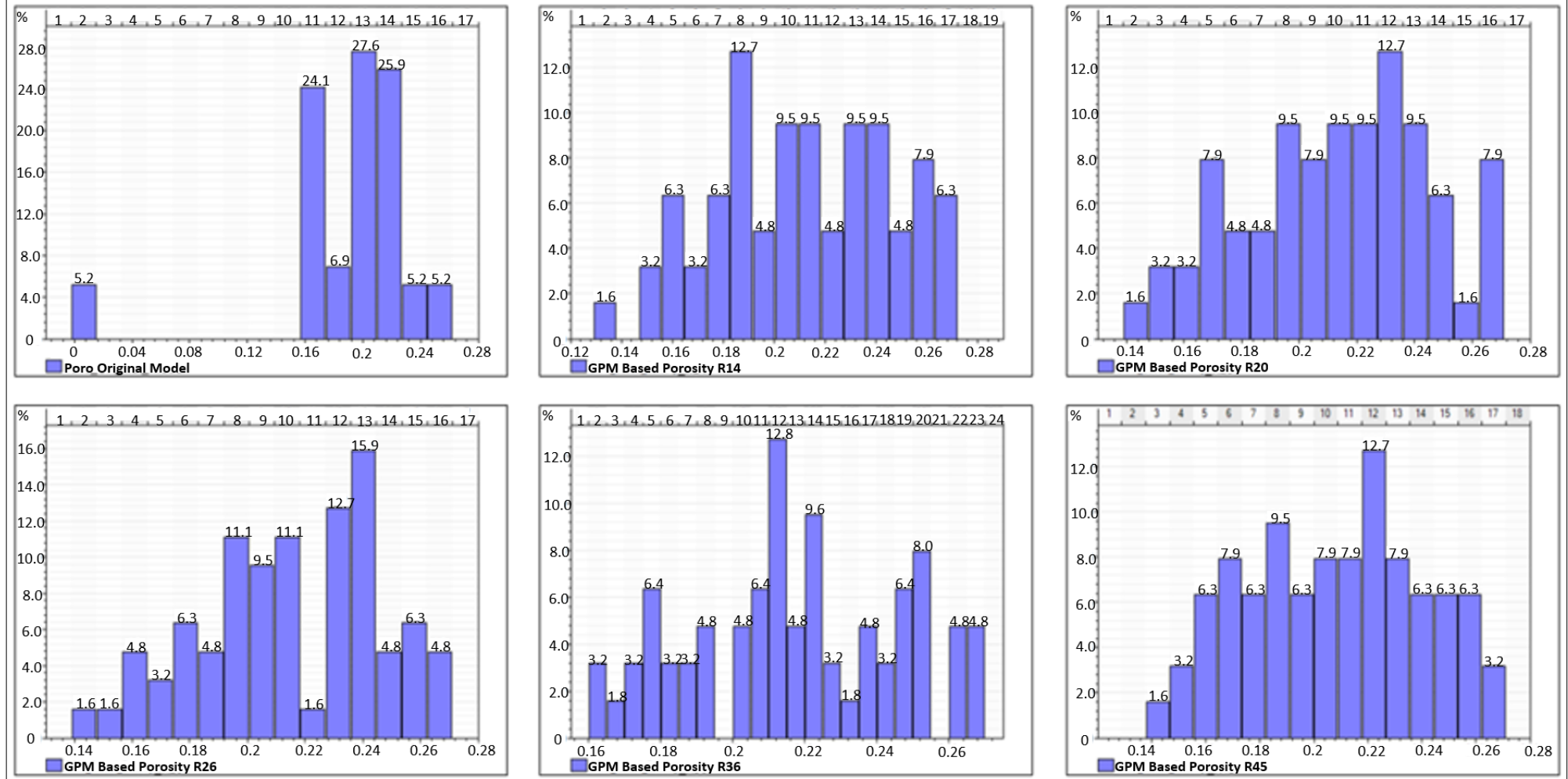


Figure 12b. Comparing porosity in validation Well 2 in five stratigraphic-based realizations, and the original model at similar vertical intervals.

Table 1 Lithofacies-associations in the Hugin formation, Volve Field (after Kieft et al. 2011).

Code	Facies	Description	Thickness (t); Extent (l)	Wireline-log Attribute	Interpretation
A	A1	Parallel-laminated mudstone with occasional siltstone inputs. Monospecific pattern of disorder bivalves parallel to bedding.	t = 30 - 425 cm l = 6 - 29 km	GR = 41 - 308 API DT = 225 - 355 μsm^{-1} NPHI = 0.17 - 0.45 v/v RHOB = 2280 - 2820 gcm^{-1}	Restricted marine shale
	A2	Inter-bedded claystone and very fine-grained sandstone; non-parallel and wavy lamination. Scarcely bivalve shells oriented parallel to bedding.	t = 10 - 725 cm l = 8 - 13 km	GR = 17 - 65 API DT = 189 - 268 μsm^{-1} NPHI = ? RHOB = 2280 - 2820 gcm^{-1}	Muddy hallow bay fill
	A3	Fine to medium grained sandstone; moderately to well sorted grain. Wavy bedding, cross bedding, rare wave ripples.	t = 60 - 370 cm l = 1 - 8 km	GR = 18 - 46 API DT = 199 - 268 μsm^{-1} NPHI = 0.07 - 0.52 v/v RHOB = 1690 - 2745 gcm^{-1}	Sandy shallow bay fill
	A4	Parallel-laminated mudstone with occasional siltstone inputs. Monospecific pattern of disorder bivalves parallel to bedding.	t = 30 - 425 cm l = 6 - 29 km	GR = 7 - 35 API DT = 175 - 230 μsm^{-1} NPHI = 0.04 - 0.15 v/v RHOB = 2280 - 2820 gcm^{-1}	Marine channel fill sandstone
B	B1	Upward coarsening siltstone to fine-grained; moderatley sorted sandstone. Shell debris and quartz granules.	t = 30 - 480 cm l = 1 - 2 km	GR = 18 - 80 API DT = 168 - 291 μsm^{-1} NPHI = 0.04 - 0.191 v/v RHOB = 2322 - 2723 gcm^{-1}	Distal lower shoreface
	B2	Very fine-fine grained sandstone. Moderate to well sorted; fine grained carbonaceous laminae, typically low angle cross beds.	t = 130 - 440 cm l = 1.7 - 12 km	GR = 20 - 56 API DT = 179 - 277 μsm^{-1} NPHI = 0.05 - 0.168 v/v RHOB = 2314 - 2696 gcm^{-1}	Proximal lower shoreface
	B3	Coarsening upward, cross laminated, fine to medium grained sandstone; consist of carbonaceous fragments.	t = 425 - 800 cm l = 1.7 - 8 km	GR = 15 - 25 API DT = 250 - 275 μsm^{-1} NPHI = 0.09 - 0.113 v/v RHOB = 2271 - 2342 gcm^{-1}	Upper shoreface
C	C1	Highly bioturbated siltstone to very fine sandstone, with beds of rounded granules.	t = 175 - 1010 cm l = 7.2 - 19.6 km	GR = 20 - 80 API DT = 230 - 260 μsm^{-1} NPHI = 0.08 - 0.169 v/v RHOB = 2327 - 2521 gcm^{-1}	Distal mouth bar
	C2	Very fine to fine grained sandstone, low angle cross bedding.	t = 290 - 775 cm l = 1 - 5 km	GR = 12 - 58 API DT = 167 - 397 μsm^{-1} NPHI = 0.05 - 0.595 v/v RHOB = 1612 - 2705 gcm^{-1}	Proximal mouth bar
D	D1	Fining upward coarse to fine grained sandstone. Stacked fining upward beds with rare coarse grained stringers.	t = 740 - 820 cm l = 1 - 2 km	GR = 8 - 134 API DT = 235 - 335 μsm^{-1} NPHI = 0.14 - 0.46 v/v RHOB = 2284 - 2570 gcm^{-1}	Tidal influenced fluvial channel fill sandstone
	D2	Fining upward coarse to medium grained sandstone. Carbonaceous laminae and fragments. Sharp and cohesive contact at base of bed.	t = 580 cm l = < 2 km	GR = 9 - 34 API DT = 241 - 297 μsm^{-1} NPHI = 0.14 - 0.289 v/v RHOB = 2168 - 2447 gcm^{-1}	fluvial channel fill sandstone
E	E1	Coal and carbonaceous shale. Basal contact typically parallel, although maybe undulose.	t = 30 - 520 cm l = 6 - 19.6 km	GR = 8 - 56 API DT = 313 - 427 μsm^{-1} NPHI = 0.24 - 0.529 v/v RHOB = 1930 - 2225 gcm^{-1}	Coal
	E2	Alternating dark grey mudstone/claystone and siltstone to very fine grained sandstone. Wavy to non-parallel lamination.	t = 60 cm l = < 2 km	GR = 32 - 60 API DT = 358 - 415 μsm^{-1} NPHI = 0.43 - 0.49 v/v RHOB = 1994 - 2148 gcm^{-1}	Coastal plain fines
F	F	Mudstone with rare siltstone beds. Parallel lamination, soft sediment deformation developed locally on top of beds.	t = section tot completely penetrated l = 1.7 - 36.7 km	GR = 4 - 134 API DT = 187 - 450 μsm^{-1} NPHI = 0.114 - 0.618 v/v RHOB = 1730 - 2925 gcm^{-1}	Open marine shale

Table 2. Input parameters for forward stratigraphic simulations in GPM™

		Initial Conditions- GPM Input Parameters												
		Simulation Duration	Sediment Type Proportion (%)				Avg. Water Velocity	Avg. Sediment Velocity	Erodibility	Diffusion Coefficient	Avg. Sea Level	Turbidite Event Interval	Steady Flow Iteration	Sediment Movement
GPM Scenarios (GS)		(Ma– 0a) Years	Sand (Coarse)	Sand (Fine)	Silt	Clay	(m/a)	(m/a)			Interval (m)	(/years)	(/hrs)	Coefficient
	S1	0.02 – 0	25	25	25	25	0.11	0.03	0.35	0.11	30	2500	10	0.001
	S2	0.25 – 0	25	25	25	25	0.15	0.03	0.45	0.15	70	1000	15	0.012
	S3	0.5 – 0	25	25	25	25	0.11	0.02	0.55	0.11	120	1000	20	0.012
	S4	0.7 – 0.05	25	25	25	25	0.08	0.02	0.35	0.08	100	500	25	0.0011
	S5	1.5 – 0	15	35	30	20	0.15	0.04	0.50	0.15	80	5000	20	0.001
	S6	3.0 – 0	50	25	15	10	0.13	0.04	0.50	0.13	70	5000	30	0.0012
	S7	3.5 – 0	50	25	15	10	0.11	0.04	0.50	0.11	70	10000	15	0.001
	S8	4.0 – 0	50	25	15	10	0.13	0.04	0.50	0.13	90	5000	20	0.0015
	S9	4.5 – 0	15	45	25	15	0.1	0.02	0.45	0.1	50	10000	30	0.0012
	S10	5.0 – 0	15	45	25	15	0.12	0.02	0.45	0.12	55	10000	35	0.0013
	S11	5.5 - 0	15	45	25	15	0.12	0.02	0.45	0.12	40	5000	40	0.0013
	S12	6.0 – 0	15	45	25	15	0.1	0.02	0.45	0.1	60	10000	35	0.0011
	S13	6.5 – 0	10	25	55	10	0.13	0.03	0.48	0.13	100	20000	50	0.0010
	S14	7.0 – 0	10	25	55	10	0.16	0.03	0.48	0.16	40	20000	45	0.0011
	S15	7.5 – 0	10	25	55	10	0.13	0.03	0.48	0.13	40	20000	40	0.0012
	S16	8.0 – 0	10	25	55	10	0.15	0.03	0.48	0.15	30	10000	30	0.0010
	S17	8.5 – 0	10	25	45	20	0.14	0.02	0.45	0.14	50	50000	50	0.0010
	S18	9.0 – 0	30	30	18	22	0.13	0.02	0.52	0.13	60	25000	35	0.0012
	S19	9.5 – 0	30	40	12	18	0.12	0.02	0.55	0.12	55	25000	20	0.0013
	S20	10.0 - 0	30	42	18	10	0.11	0.01	0.40	0.11	50	5000	15	0.0011
Sediment Property														
	Sediment Type	Diameter	Density	Initial Porosity	Initial Permeability	Compacted Porosity	Compaction	Compacted Permeability	Erodibility					
	Coarse Grained Sand	1.0 mm	2.70 g/cm ³	0.21 m ³ /m ³	500 mD	0.25 m ³ /m ³	5000 KPa	50 mD	0.6					
	Fine Grained Sand	0.1 mm	2.70 g/cm ³	0.3 m ³ /m ³	100 mD	0.15 m ³ /m ³	2500 KPa	5 mD	0.45					
	Silt	0.01 mm	2.65 g/cm ³	0.38 m ³ /m ³	50 mD	0.12 m ³ /m ³	1200 KPa	2 mD	0.3					
	Clay	0.001 mm	2.65 g/cm ³	0.48 m ³ /m ³	5 mD	0.05 m ³ /m ³	500 KPa	0.1 mD	0.15					

Table 3. Lithofacies classification in the forward stratigraphic model in the property calculator tool in Petrel™.

Lithofacies Classification		
Facies Code	Lithofacies	Command Used in Petrel's Property Calculator
0	Marine Shale	If(Sand_fine>=0.19 And Sand_fine<=0.21 Or Silt>=0.19 And Silt<=0.2 Or Clay>=0.2 And Clay<=0.21 Or Depth_of_deposition>=-82 And Depth_of_deposition<=-78)
1	Muddy Shallow Bay Fill	If(Sand_fine>=0.36 And Sand_fine<=0.38 Or Silt>=0.18 And Silt<=0.2 Or Clay>0.18 And Clay<=0.19 Or Depth_of_deposition>=-30 And Depth_of_deposition<=-20)
2	Sandy Shallow Bay Fill	If(Sand_coarse>=0.65 And Sand_coarse<=0.73 Or Sand_fine>=0.18 And Sand_fine<=0.22 Or Silt>=0.18 And Silt<=0.2 Or Clay>=0.17 And Clay<=0.18 Or Depth_of_deposition>=-3 And Depth_of_deposition<=0)
3	Channel Fill Sandstone	If(Sand_coarse>=0.5 And Sand_coarse<=0.68 Or Sand_fine>=0.23 And Sand_fine<=0.25 Or Silt>=0.17 And Silt<=0.18 Or Depth_of_deposition>=0 And Depth_of_deposition<=2)
4	Lower Shoreface Units	If(Sand_coarse>=0.19 And Sand_coarse<=0.31 Or Sand_fine>=0.19 And Sand_fine<=0.24 Or Silt>=0.4 And Silt<=0.48 Or Clay>=0.19 And Clay<=0.31 Or Depth_of_deposition>=-83 And Depth_of_deposition<=50)
5	Middle Shoreface Units	If(Sand_coarse>=0.32 And Sand_coarse<=0.53 Or Sand_fine>=0.25 And Sand_fine<=0.32 Or Silt>=0.26 And Silt<=0.32 Or Clay>=0.19 And Clay<=0.21 Or Depth_of_deposition>=-38 And Depth_of_deposition<=-12)
6	Upper Shoreface Units	If(Sand_coarse>=0.53 And Sand_coarse<=0.72 Or Sand_fine>=0.28 And Sand_fine<=0.33 Or Silt>=0.16 And Silt<=0.21 Or Depth_of_deposition>=-10 And Depth_of_deposition<=6)
7	Distal Mouth Bar Units	If(Sand_fine>=0.23 And Sand_fine<=0.27 Or Silt>=0.38 And Silt<=0.43 Or Clay>=0.19 And Clay<=0.21 Or Depth_of_deposition>=-95 And Depth_of_deposition<=-80)
8	Proximal Mouth Bar Units	If(Sand_coarse>=0.53 And Sand_coarse<=0.71 Or Sand_fine>=0.27 And Sand_fine<=0.32 Or Silt>=0.16 And Silt<=0.21 Or Clay>=0.06 And Clay<=0.07 Or Depth_of_deposition>=-30 And Depth_of_deposition<=-27)
9	Tide Influenced Sandstones	If(Sand_coarse>=0.53 And Sand_coarse<=0.71 Or Sand_fine>=0.26 And Sand_fine<=0.31 Or Silt>=0.35 And Silt<=0.41 Or Depth_of_deposition>=-5 And Depth_of_deposition<=1)
10	Fluvial Channel Sandstones	If(Sand_coarse>=0.54 And Sand_coarse<=0.56 Or Sand_fine>=0.27 And Sand_fine<=0.29 Or Silt>=0.19 And Silt<=0.21 Or Depth_of_deposition>=-2 And Depth_of_deposition<=2)
11	Coal	Estimated as background attribute
12	Coastal plain fines	If(Silt>=0.31 And Silt<=0.43 Or Clay>=0.31 And Clay<=0.35 Or Depositional_depth>=-100 And Depositional_depth<=-40)
13	Marine Mudstone	If(Sand_fine>=0.36 And Sand_fine<=0.38 Or Silt>=0.4 And Silt<=0.52 Or Clay>=0.45 And Clay<=0.78 Or Depth_of_deposition>=-105 And Depth_of_deposition<=-90)

Table 4. Porosity and Permeability estimates of lithofacies packages in the model area.

Code	Lithofacies	Avg. NPHI	Density Porosity	Estimated Porosity	KLOGH (mD)
0	Marine Shale	0.17 - 0.45	0.1	0.08 - 0.11	10.02 - 16.1
1	Muddy Shallow Bay Fill	0.17 - 0.42	0.1	0.08 - 0.13	23.85 - 102.3
2	Sandy Shallow Bay Fill	0.07 - 0.52	0.25	0.16 - 0.25	100.0 - 398.7
3	Channel Fill Sandstone	0.04 - 0.15	0.3	0.18 - 0.22	400.01 - 889.7
4	Distal Lower Shoreface	0.04 - 0.19	0.29	0.1 - 0.23	120.5 - 170.3
5	Proximal Shoreface	0.05 - 0.17	0.31	0.17 - 0.24	80.2 - 412.5
6	Upper Shoreface	0.09 - 0.11	0.28	0.21 - 0.26	650.2 - 1023.7
7	Distal Mouth Bar	0.08 - 0.17	0.27	0.09 - 0.17	170.5 - 223.1
8	Proximal Mouth Bar	0.05 - 0.59	0.12	0.19 - 0.21	130.5 - 314.3
9	Tidal Influenced Sandstone	0.14 - 0.46	0.26	0.15 - 0.20	220.0 - 512.6
10	Fluvial Sandstones	0.14 - 0.29	0.21	0.19 - 0.21	180.5 - 691.8
11	Coal	0.24 - 0.53	0.05	0.001	0.001
12	Coastal Plain Fines	0.43 - 0.49	0.06	0.04 - 0.12	5.2 - 34.6
13	Marine Mudstone	0.16 - 0.42	0.1	0.08 - 0.10	6.0 - 15.2

Table 5. A comparison of a) porosity, and b) permeability estimates from selected intervals in the original porosity/permeability models and forward modeling-based porosity and permeability models.

a. Validation Well Position 1					
	Depth (m)				
	5 m	10 m	15 m	25 m	35 m
Models	Measured Porosity				
Original Model	0.2	0.25	0.27	0.16	0.13
R14	0.22	0.24	0.16	0.22	0.16
R20	0.16	0.19	0.26	0.18	0.15
R26	0.18	0.17	0.23	0.16	0.19
R36	0.22	0.21	0.19	0.22	0.21
R45	0.25	0.2	0.23	0.22	0.15
R49	0.21	0.17	0.22	0.17	0.18
Validation Well Position 2					
	Depth (m)				
	5 m	10 m	15 m	25 m	35 m
Models	Measured Porosity				
Original Model	0.17	0.21	0.21	0.17	0.19
R14	0.17	0.16	0.24	0.15	0.25
R20	0.21	0.22	0.2	0.21	0.23
R26	0.21	0.2	0.21	0.25	0.24
R36	0.2	0.22	0.21	0.21	0.19
R45	0.22	0.19	0.2	0.19	0.21
R49	0.26	0.24	0.23	0.16	0.21
b. Validation Well Position 1					
	Depth (m)				
	5 m	10 m	15 m	25 m	35 m
Models	Measured Permeability_Z (mD)				
Original Model	352.74	312.38	201.08	199.76	508.2
R14	163.95	312.38	69.84	310.16	508.2
R20	290.84	315.09	105.66	273.04	200.63
R26	375.92	203.81	166.23	189.92	348.12
R36	418.03	203.27	190.9	168.9	370.56
R45	337.6	412.67	199.66	156.71	305.92
R49	370.89	129.33	291.77	175.53	551.18
Validation Well Position 2					
	Depth (m)				
	5 m	10 m	15 m	25 m	35 m
Models	Measured Permeability_Z (mD)				
Original Model	6.6	883.6	30.3	496.99	156.6
R14	320.34	336.22	151.08	464.22	132.98
R20	122.66	209.15	161.3	230.58	208.48
R26	151.48	710.07	175.09	384.49	169.48
R36	184.74	344.99	157.08	420.15	136.14
R45	91.44	361.04	77.17	382.85	134.56
R49	134.01	721.73	137.42	636.48	290.06